Volume 11
Number 21
7 November 2021
Pages 6893–7218

Catalysis Science & Technology

rsc.li/catalysis

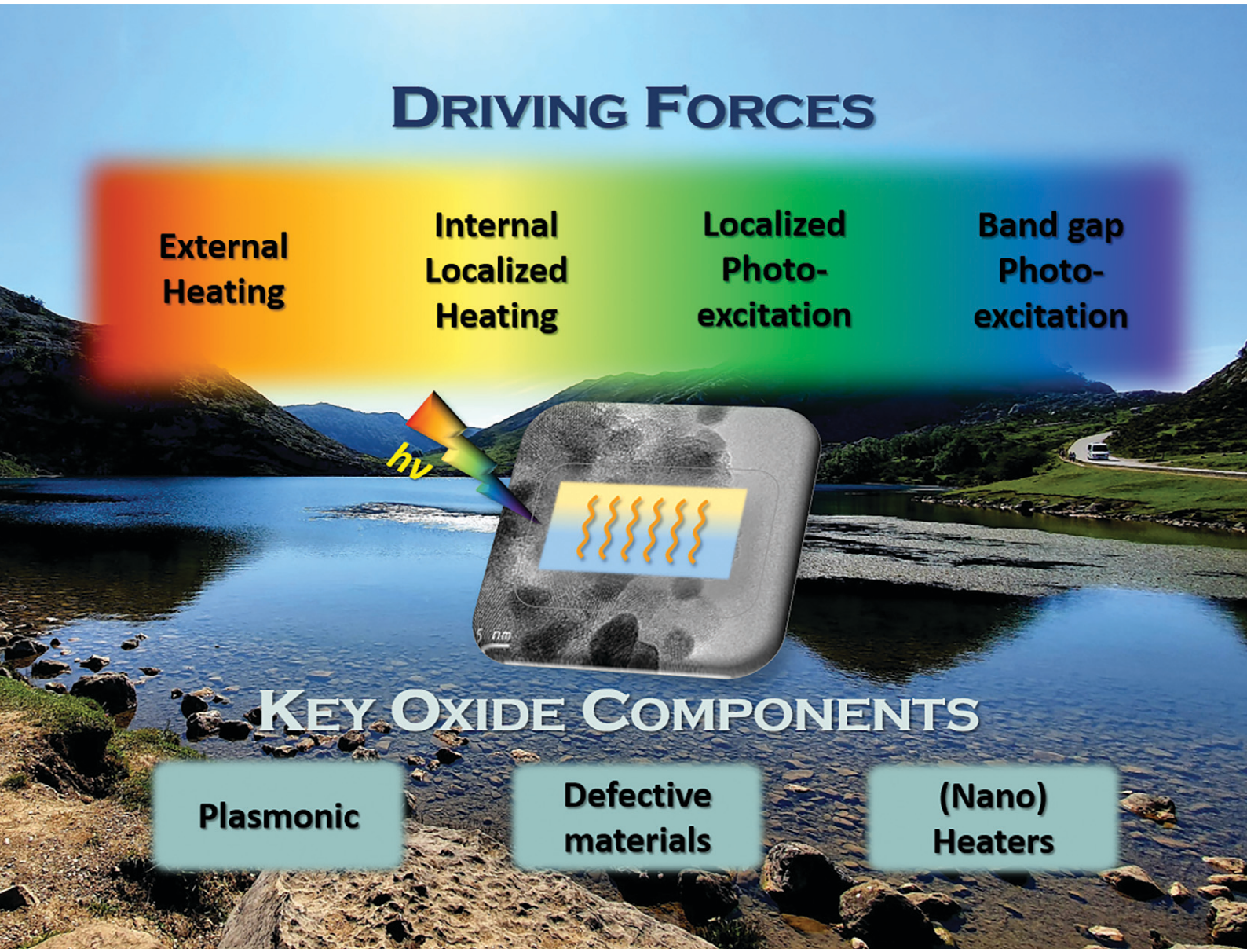

ISSN 2044-4761

ROYAL SOCIETY OF CHEMISTRY

MINIREVIEW
Anna Kubacka, Marcos Fernández-García *et al.*
Oxide-based composites: applications in thermo-photocatalysis

Catalysis Science & Technology

ROYAL SOCIETY OF CHEMISTRY

MINI REVIEW

View Article Online
View Journal | View Issue

Cite this: *Catal. Sci. Technol.*, 2021, 11, 6904

Oxide-based composites: applications in thermo-photocatalysis

Irene Barba-Nieto,† Natividad Gómez-Cerezo,† Anna Kubacka * and Marcos Fernández-García *

The combination of thermal and photonic energy sources to carry out catalyzed chemical reactions appears as a new avenue to optimize the current industrial-oriented processes as well as to open new ones. Herein, we analyze the contribution of novel oxide-based composite systems to the thermo-photocatalysis field. In the first place, the review article gives a brief introduction about the physicochemical framework to interpret the thermo-photocatalytic properties of oxide-based solids. From this point and to provide an overview of the progress of the field, we classify the oxide-active catalysts in three main categories considering materials with catalytic properties primarily governed by plasmonic, defect-related, and thermal effects. For each type of system, we analyze the representative oxide systems and the corresponding composite systems, emphasizing the study on the interpretation of the catalytic behavior. The contribution ends with a summary of the current status and an outlook into the future of the field.

Received 15th June 2021,
Accepted 8th September 2021

DOI: 10.1039/d1cy01067k

rsc.li/catalysis

1. Thermo-photocatalysis: a new word

As is well-known, thermal or classical catalysis considers the transformation of molecules through the potential energy surface characteristic of the ground electronic state of the catalyst. The transformation can be more or less complex but the key concepts are the thermodynamic feasibility of the reaction (without relation to the catalyst) and the energy barrier of the (kinetically-relevant) rate-limiting step of the reaction. The catalyst mainly decreases the latter observable, reducing the energy consumption and time for reaction, or, in other words, increasing the reaction rate. Also, through the effect exerted in the different reaction steps, it may control or the influence selectivity. Thermal energy normally allows the reactant(s) to obtain enough energy to overcome the activation energy through vibrational coupling between the phonons of the catalytic solid and localized levels of the reactants. The operational variables (temperature and pressure in most cases) affect the adsorption/desorption and surface coverage of the reactant, intermediates, and products.[1] In the case of photocatalysis, the excited energy levels of the catalyst shape the potential energy surface of the reaction. Light allows the access of the system to such excited states of the solid. Charge carriers (electrons and holes) generated after light absorption simultaneously access the specific electronic levels of the excited states. After reaching the surface of the solid, the charge carrier species can interact (if thermodynamically feasible[2]) with the reactants and/or other molecules, intermediates, or oxygen in the case of degradation or selective oxidation reactions.[3] Recombination competes with these steps. Obviously, the energy barriers of thermal and photo-triggered processes for the same chemical reaction are distinct as they take place at different potential energy surfaces. Moreover, the de-excitation processes are different, while the thermal ones are (dominantly) adiabatic and the light-induced ones are not adiabatic in nature. Thus, there is not surprise on obtaining different reaction rates and selectivities.

Instituto de Catálisis y Petroleoquímica, CSIC, Marie Curie 2, 28049 Madrid, Spain. E-mail: ak@icp.csic.es, mfg@icp.csic.es
† Authors contributing equally to this work.

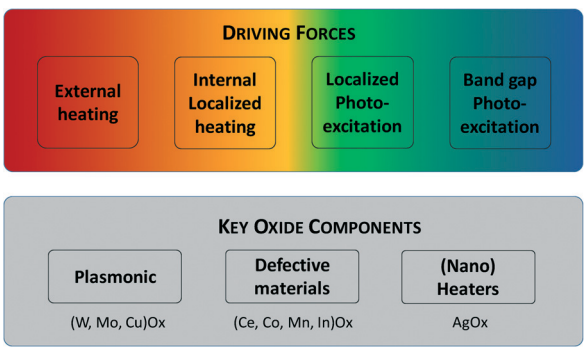

Fig. 1 Schematic representation of the driving forces and the key components of thermo-photo(composite) catalysts.

Among catalysts, particularly photocatalysts, oxides are of primary importance. To use light efficiently, they need to be semiconductors as they have the required electronic properties to limit charge recombination after light excitation. Titanium oxide is the central system in photocatalysis as it displays outstanding activity in most of the reaction tested.[3] When light and heat are used simultaneously with a catalyst, the energy framework where the process occurs is significantly more complicated, at least from the physical point of view. The first point comes from the fact that energy can be transferred to the solid in several ways. As depicted in Fig. 1(upper panel), the thermal energy can be transferred to the catalyst using external heating (the conventional procedure in catalysis) or heating derived from charge carrier species recombination. Note that even in the case of the more effective photocatalyst such as titania and considering nanoparticulate materials (*i.e.*, high surface area catalysts), above 90–95% of the excited charge carriers recombine, generating mainly heating (geminate and non-geminate non-radiative recombination).[3] Thus, heating is inherent to any photocatalytic process and cannot be decoupled.

At the same time and within the context of thermo-photocatalysis, we can make a useful difference based on the absorption of the photons using band or localized electronic states (Fig. 1; upper panel). Active photocatalysis mostly (although not exclusively) use valence to conduction band transition(s) due to the higher absorption (extinction) coefficient with respect to the one connected with the transitions related, in one way or other, with at least one localized state, as well as the more efficient control of recombination. From classic thermodynamics, it is easy to prove that valence to conduction band electronic transition(s) cannot be affected by the temperature and are thus essentially not useful for thermo-photocatalysis. Nevertheless, even for semiconductor materials working exclusively with band-type light-triggered electronic transitions (a phenomenon that rarely takes place in nanosized materials as the defect structure is considered key to control the photoactivity), the temperature affects some of the physical phenomena primarily considered as light-driven. These are charge carrier mobility and, to a certain degree (particularly related to photon–phonon coupling), charge recombination. Of course, to this, we can add the surface coverage of the relevant chemical species.[4–6]

For the purpose of combining light and heat, catalytically relevant light-triggered electronic transitions can be classified according to the main use of photon or thermal energy (Fig. 1; bottom panel). In this contest, photon-type main physical phenomena utilized are related to the use of the plasmonic or defect-controlled components. In both the cases, the heating connected effects are well-described (inherent to the photonic phenomenon) and their significance under discussion. On the contrary, (nano-) heater materials could be the mainly thermally-oriented component of thermo-photo materials (Fig. 1; bottom panel). The inclusion of such materials in composite catalysts can trigger a strong thermal gradient across the solid. In the context of this contribution, mainly low-energy gap oxides (having band gap energy fitting with IR excitation) have been used as (nano)heaters but other possibilities will be briefly discussed herein.[7–11]

Besides the above-mentioned phenomena primarily related to the catalyst, we cannot forget that mixing thermal and photonic energy can alter the adsorption/desorption, surface coverage, and/or create specific intermediate or reactive species absent in the case when using a single energy source and are thus specific for the combination.[3,4,6]

Oxide-based composite materials can be, and are frequently, designed toward the simultaneous use of several of the above-mentioned physicochemical phenomena taking place under combined thermo-photo excitation. This contribution is dedicated to the analysis of the above-mentioned composite catalysts, focusing on the study of the role of the oxide components. It would complement previous works centered on analyzing the metal components of thermo-photocatalysts.[11] Before considering the active systems that accomplish such a task, we can have a simple picture of the handling of thermal and light energy by plasmonic, defect-related, and (nano)heat oxide-based systems. We would thus classify the main thermo-photo component(s) of oxide-based composite materials as being in one of these three categories (Fig. 1; bottom panel). Again, we stress that the classification emerges from a simple picture, aiming to outline the basic framework for the interpretation of the catalytic results. We also claim that commonly, several of the physicochemical phenomena mentioned work simultaneously. At least, each one of these three types of systems mentioned has specific (thermo-photo) phenomenon taking place not only at the catalytic solid but also at the catalyst–reactant interface.

Plasmonic oxides utilized in the field are essentially those related to WO_{3-x}, MoO_{3-x}, and Cu_2O_x systems.[11,12] These oxide systems can possess metallic-band type electronic structure originated by the partial filling of the (stoichiometric oxide) valence/conduction band by downward (Cu)/upward (W, Mo) shift of the Fermi edge. However, in the cases of Mo and Cu (pure, non-doped) oxides, it might also be associated to the surface (strongly reduced) structures albeit the situation is still far from clear. The electronic structure taking part in cation doping of these oxide systems and facilitating the plasmonic behavior is more complex.[10,12,13] It is obvious that the described plasmonic oxide materials are in one way or another (strongly) defective but their electronic structure would command their catalytic properties. In composite systems, visible and infrared light can induce electron oscillations at the (plasmonic/non-plasmonic) interface of composite semiconductor-based systems and this is the physical phenomenon governing charge transfer through the corresponding interface. Among plasmonic modes, photocatalysis can benefit from the so-called localized surface plasmon resonance(s), which are

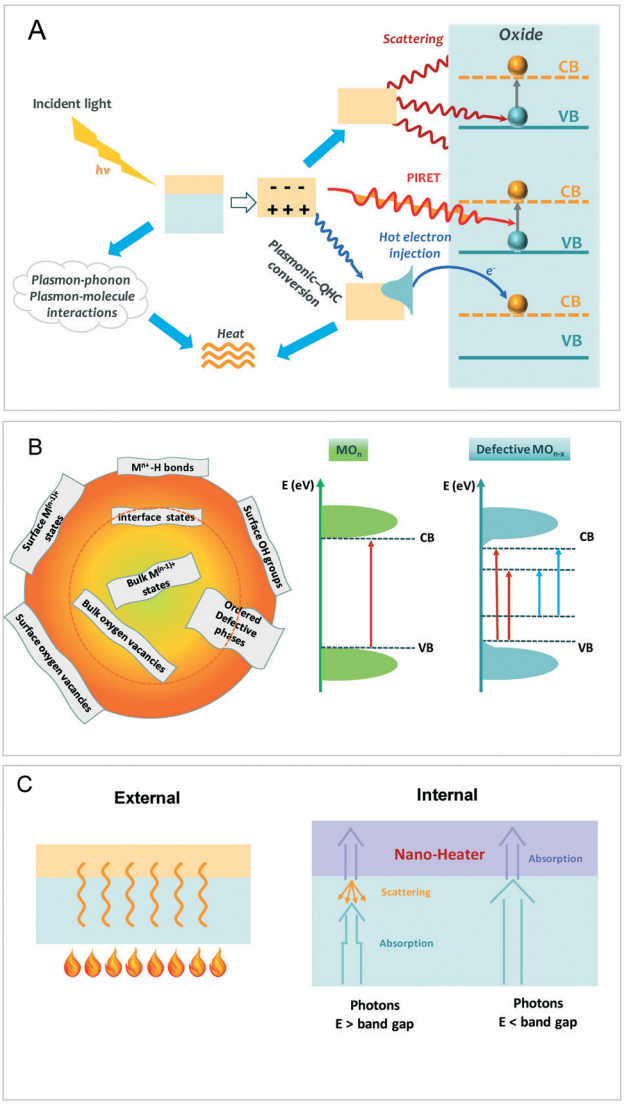

Fig. 2 Schematic representation of the main types of thermo-photo composite catalysts having plasmonic (A), defect-engineering (B), and (nano)-heating (C) components.

collective oscillations of free electrons generated under illumination and localized in a small region. As illustrated in Fig. 2A, plasmons can modulate photocatalysis through several phenomena: i) strong light absorption; ii) intense far-field light-scattering; iii) near-field electromagnetic field strengthening, iv) increase of hot carrier generation; and v) heating effects.[14,15] Scattered photons can suffer absorption by the (non-plasmonic) semiconductor and can be subsequently utilized in photocatalysis (this phenomenon is sometimes called the trapping of light). Scattered light would be absorbed or not absorbed depending on its wavelength and the main oxide (such as titania) band gap energy (Fig. 2A; upper part). Plasmons can also generate dipole moments (having significantly inferior magnitude than the one for plasmonic metals). The non-radiative transference of plasmonic energy can take place at a semiconductor/oxide in the near-field zone through the dipole–dipole interaction. This phenomenon will subsequently lead to the generation of electron–hole pairs. The so-called plasmon-induced resonance energy transformation (PIRET) can occur even in the presence of an insulating component in contact with the plasmonic component (Fig. 2A; middle part). The plasmon resonance non-radiative decay occurring after light absorption generates, through Landau damping, a high-energy quantum hot charge (QHC) carrier. These carrier species can be injected into the conduction band of the (main) semiconductor/oxide after surpassing the interface barrier (Fig. 2A; bottom part). The detailed analysis of these phenomena indicates a strong influence of the size and shape of the plasmonic material in these processes.[15,16] Finally, through plasmon–phonon (and adsorbed molecules) interaction(s), the plasmons can decay inelastically in heat. The last event generates local hot spots. We briefly note that there are other plasmonic materials based on heavily doped oxides such as Al- or Ga-doped ZnO or Sn–In_2O_3.[17] So far, we are not aware of their use in thermo-photocatalytic applications.[7–13]

Defect-controlled thermo-photocatalysts are defective materials lacking plasmonic properties (or at least with negligible plasmonic effects on the catalytic behavior according to the literature). This means that the defect structure does not lead to a pseudo-metallic band structure by the partial filling of valence/conduction bands. Most active materials use CeO_x, CoO_x, MnO_x, BiO_x, or InO_x, although many other oxides have been essayed. In general, these oxide materials can accommodate anion vacancies (with cation-associated oxidation state alteration in most cases) and display significant defect (thermal) mobility, promoting a fluid surface-bulk defect exchange. The thermo-photo activity of these defect-type oxide materials is also frequently studied at the oxide–oxide interfaces, particularly with titania.[7–12] The exact way that the defects are formed and evolve under external variables (mainly temperature and light) are distinctive for each system. The most common structural defects and associated localized electronic states either above and/or below the Fermi edge are schematically presented in Fig. 2B. Some of these defect-derived electronic states are optically active, allowing (light-triggered) excitation. The critical role of these electronic states is, in general, related to their role in charge localization after excitation combined with the fact that they (and/or associated reduced cations) frequently have activity in thermal (alone) steps. Moreover, as mentioned, they are particularly relevant for driving the catalytic behavior of oxide–oxide interfaces.[7] In addition, strongly defective oxides can lead to the so-called black systems. Ideally, black oxide materials could be well suited to handle light and heat after sunlight excitation, profiting from the whole electromagnetic range. In addition of generating localized electronic states, it may alter the valence/conduction density of states distribution from the corresponding (non-black, sometimes called white) reference materials (Fig. 2B). Black titania is the most studied material

but the interpretation of its catalytic behavior is under heavy discussion. Nevertheless, the most recent general discussions point out that the photon-triggered activity in this system comes from an improved defect-related handling of the UV photons, with relatively low efficiency for visible or infrared photons.[18] Thus, the use of heavily defective materials in the context of a purely photon-related thermo-photo phenomenon is an open question. To date, it appears that black-type systems have limited advantages to be exploited in photonic/thermal-triggered processes yet some relevant examples are presented in relation to specific oxides such as indium oxide.

For (nano)heating-based materials, we can consider catalytic systems where such components are specifically delineated in order to profit from heat supplied either from external (typical conduction and/or convection heating) or internal (light-related) heating (Fig. 1). Again, this property can be shared by a lot of the previously mentioned composite systems but, here, we would focus on those materials where this property is critical for enhancing the activity. In Fig. 1, we described internal heating in a general way but it can have a local or non-local nature and can be based in several different physicochemical phenomena. They will be explained in the corresponding section. External heating mostly excites the phonon modes of the catalytic solid (and in specific cases vibrational modes of the adsorbed molecules) while light-related internal heating can occur *via* non-radiative de-excitation and/or by the excitation of the phonon modes of a high absorbing material (essentially having null or minor catalytic role). External heating could be utilized in combination with low to moderate light intensities while internal heating requires significantly higher light intensities to provide an appreciable enhancement of the activity.[7–12] The ideal processes taking place in composite systems designed to profit from external or internal heating are depicted in Fig. 2C. External heating is the closest to conventional catalysis. In this case, the components utilized attempt to combine (to a first approximation) good and primarily "independent" thermal and photocatalytic properties. Internal heating-oriented systems often attempt to develop designed structures with advantageous handling of the specific physical phenomena taking place for all the photons of UV-visible-IR energy sources. Typical UV-visible photons are utilized by light-active catalytic component(s) while low energy visible and near/middle IR photons are used by the (nano)heater component. Multiple optical events can take place, as schematically illustrated in Fig. 2C. Specific oxide components to develop internal heating effects in catalysts mostly concentrate on low band gap materials with dominant non-radiative de-excitation such as Ag_2O_x. A lot of other semiconductors such as Bi, Mo, Ag, Sb, W and Sn sulfides or In, and Cu selenides are used in this quest. Al, Cu, and other metals (used as foils or surfaces over which the active catalyst can be deposited) with strong visible-IR light absorptivity are also used.[7,9,12] Finally, a novel pathway attempts to use pyroelectric materials. The Seebeck effect can convert a temperature gradient into an electric field, which may be used to control and favor the separation of charge carriers as well as the subsequent migration.[19] Some oxides such as $ZnSnO_3$ show enhanced photocatalytic properties under cycling temperature treatments.[20] Although somehow out of our scope, we can mention that piezoelectric materials can be stressed by pressure, leading to an imbalance of charge and thus allowing the conversion of mechanical energy (with inherent thermal losses) into an electric field, which may be used to control the charge carrier behavior under illumination.[21] Some oxides such as $Bi_4Ti_3O_{12}$ have been tested in this context.[22]

In this review, we will consider the three types of systems described in Fig. 2, focusing our attention on composite systems with oxide components playing a major role. We have organized each section, analyzing the most representative oxide systems studied in the literature. Attention is paid to analyze the critically representative examples of the application rather than an exhaustive survey of the literature.

2. Plasmonic oxides

In the 2010s, localized surface plasmon resonance (LSPR) attracted the attention of scientific community due to its potential applications such as photovoltaics,[23,24] surface-enhanced Raman scattering sensing,[25,26] photothermal actuators,[27,28] and photocatalysis.[29–31] One of the most interesting applications of LSPR is enhancing visible or near infrared light activity in photocatalysis.[14,29,32,33] In this context, the main charge-handling mechanism of plasmon-based composite materials is presented in Fig. 2A. LSPR has been mostly associated with noble metals, *e.g.*, Ag, Au, and Pt, but the high cost, limited availability, and complex preparation procedure have motivated the study of new strategies.[34–36] Even though most of the plasmonic thermo-photocatalytic systems include metal in their structures, some systems with the LSPR effect in the visible and near-infrared (NIR) region have been observed using metal oxide nanostructures. In particular, non-stoichiometric transition-metal oxide semiconductors, such as WO_{3-x}, and MoO_{3-x} or Cu_2O show plasmonic activity, motivating many different strategies to design systems with thermo-photoactivity.[37–39] Other plasmonic oxides such as RuO_x have been investigated only in a few cases in the context of thermo-photocatalysis. For example, a core–shell RuO_x–Ru structure deposited over titania was found to handle the efficiency of thermal and photonic phenomena to strongly boost the production of hydrogen from biomolecules.[36] Semiconductor plasmon materials present several advantages compared to noble metal plasmonic materials, such as (the above-mentioned) low in cost, higher versatility, and broad-spectrum use from visible to near (NIR) and mid-infrared (MIR) region.

WO_{3-x}-Based systems

In the past few years, tungsten-based systems have been deeply studied. Among metal oxides with oxygen vacancies, a wide range of substoichiometric WO_{3-x} systems, including $WO_{2.72}$ ($W_{18}O_{49}$), $WO_{2.8}$ (W_5O_{14}), $WO_{2.83}$ ($W_{24}O_{68}$), and $WO_{2.9}$ ($W_{20}O_{58}$), have been synthesized.[40] In general, they are thermodynamically (and cation oxidation state) stable up to 400 °C and they all present thermo-photocatalytic activity.[10,41] Usually, plasmonic WO_{3-x} are colored materials synthesized using hydrothermal methods, which allows high control of the final structure.

The thermo-photocatalytic effect has been occasionally described in mesoporous WO_{3-x} through oxygen vacancies. For instance, inducing vacancies by different H_2 treatments in WO_{3-x} improved the reduction of CO_2. The mechanism described the presence of oxygen-containing species on the surface, which decreased the WO_3-type band gap energy and increased the thermo-photocatalytic performance.[42] Similarly, some works measured the CO_2 conversion evolution rate comparing thermo-photocatalysis and photocatalysis, which showed an enhancement in the yield with temperature.[43] The mentioned works do not explore or analyze the plasmonic effect possessed by WO_{3-x}. More focused on the plasmon-related activity, Lou *et al.* describe the solvothermal synthesis of WO_{3-x} ($W_{18}O_{49}$) nanowires, from $W(CO)_6$ heated at 160 °C for 12 h in the absence of surfactants[44] (Fig. 3A–C). The synthetic method (described in Fig. 3A) allows the formation of self-doped WO_x, leading to the formation of oxygen vacancies and reduced cation oxidation states (see TEM-XPS data in Fig. 3B). As suggested by UV-visible spectroscopy (Fig. 3B), "hot" plasmonic electrons are generated after irradiation with visible and NIR, favoring charge transfer to the reagents adsorbed on the WO_{3-x} nanowire surface for hydrogen evolution (Fig. 3C). Also, the thermo-photoeffect related to the non-radiative decay of the electron oscillations may give additional localized heating on the WO_{3-x} nanowire surface, thereby enhancing the formation of H_2 from ammonia borane. However, further investigation would be necessary to elucidate the full mechanism of this reaction.[44] Several WO_{3-x} structures and morphologies, with the control of oxygen vacancies, have been synthesized as the catalyst(s) for ethanol dehydration. Fig. 3D shows XRD patterns (a), SEM and TEM images (b–g), XPS spectra (h), and UV-vis-NIR absorption spectra (i), evidencing the morphological/electronic differences between the samples. Under full-

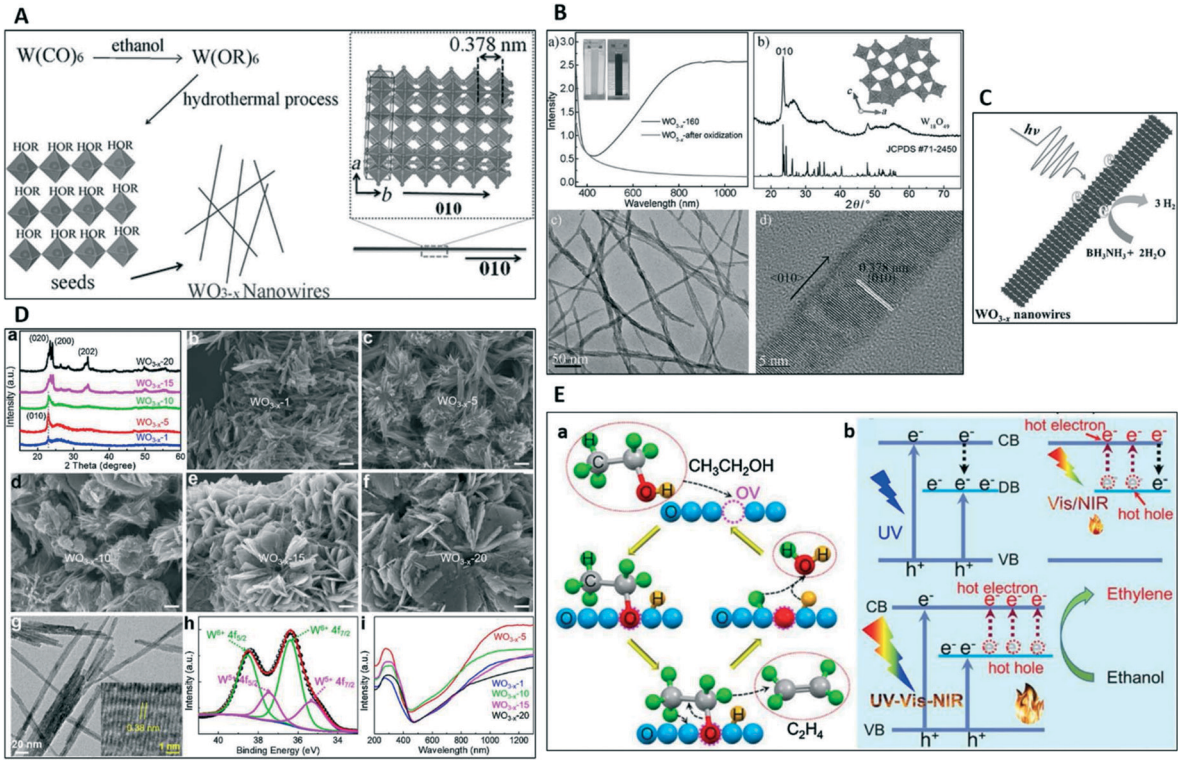

Fig. 3 A) Formation of WO_{3-x} nanowires. B) Physicochemical characterization of the WO_{3-x}-160 sample: UV/vis absorption spectra (a), XRD pattern compared with the standard $W_{18}O_{49}$ (JCPDS no. 71-2450) (b), TEM (c), and HRTEM (d) images. C) Mechanism of plasmon-enhanced H_2 evolution from BH_3NH_3 using WO_{3-x} nanowires. D) Characterization of the WO_{3-x} catalysts: XRD patterns (a) and SEM images (b–f), 200 nm (scale bar); TEM and HRTEM (inset) micrographs (g); W 4f XPS spectrum (h) (WO_{3-x}-5 sample) and UV-vis-NIR absorption spectra (i). E) Illustration of the ethanol dehydration mechanism over plasmonic WO_{3-x} (a), where: lattice oxygen (blue balls), pink circles (OVs), original positions of OVs subsequently filled with oxygen from the CH_3CHO– species (red ball with dashed pink lines), accompanying hydrogens (orange balls). Light excitation and transfer of the charge carrier species in plasmonic WO_{3-x} under UV, vis/NIR, and UV-vis-NIR light irradiation (b). A–C) reprinted from ref. 44 (copyright® Wiley 2015); D and E) reprinted from ref. 45 (copyright® Elsevier 2020).

spectrum light irradiation and compared to other structures, the defective WO_{3-x} nanowire system gives the highest ethylene production rate (16.9 mmol g^{-1} h^{-1}) with high selectivity. The plasmon-based catalytic behavior was evaluated under UV, visible, NIR, UV-vis, vis-NIR, and UV-vis-NIR irradiation. NIR increased the ethylene production, proving to have an active role of plasmonic hot electrons, apparently through a combined thermo-photoeffect.[45] Fig. 3E illustrates the proposed mechanism, which was intensively investigated, confirming the essential role of the defect-derived electronic states (DB in the figure), which, combined with enough thermal energy, favors ethanol dehydration to ethylene.

Recently, the combination of $W_{18}O_{49}$ nanofibers onto WO_3 microrods has been explored, exhibiting higher photocatalytic activity compared to the parent components for the degradation of 2,4-DCP (2,4-dichlorophenol) under NIR and full-spectrum light irradiation.[46] The experimental study of the mechanism indicated the essential role played by the holes and hydroxyl radicals under light irradiation. Electron paramagnetic resonance (EPR) studies confirmed the presence of such radical species generated by $W_{18}O_{49}$ or WO_3@$W_{18}O_{49}$, which is double the amount of hydroxyl radicals in the case of WO_3@$W_{18}O_{49}$. A plasmonic excitation takes place, presenting evidence that this pathway promotes the formation of hydroxyl radicals as an active species of the reaction. The generated electrons in $W_{18}O_{49}$ can be transferred to the CB of WO_3, increasing the charge carrier lifetime. In addition, the LSPR effect of $W_{18}O_{49}$ was more efficient (with respect to the bulk counterpart) due to the high surface exposed, ending in an enhanced activity for the full-spectrum light-driven photodegradation for 2,4-DCP.

Very often, W-containing oxides are found in the literature associated with plasmonic metals such as Au, Ag, Pd, or Pt. These systems are generally prepared by solvothermal treatment, presenting a wide range of structures and morphologies. Usually, the metal and the oxide present a synergic plasmonic activity.[42,47,48] For instance, as shown in Fig. 4, Pd–WO_{3-x} nanowires with plasmonic activity under NIR illumination have been shown to promote the Suzuki coupling reactions.[48] Also, amorphous 2D Ag/a-WO_{3-x} heterostructures fabricated *via* the supercritical CO_2 method have been proved as an interesting approach for the design of new catalysts.[49] These systems present very different morphologies (Fig. 4), confirming the versatility of the systems based on WO_{3-x} with plasmonic activity. One of the most studied WO_{3-x} material is $W_{18}O_{49}$, which displays significant plasmonic activity in contact with metallic structures for several applications.[50,51]

Even more interesting for our purposes is the application of WO_{3-x} combined with other oxides, and other semiconductors or insulators in thermo-photocatalysis,[52–56] which represents a promising alternative to decrease the use of noble materials. Following this strategy, in the past few years, different systems have been designed to test the catalytic potential of the LSPR effect.[57–59] Among tungsten-based oxide–oxide heterostructures, the combination with TiO_2 has been widely analyzed. Nevertheless, the full use of the plasmonic effect is scarcely investigated in this composite system. An example is the W,Er-codoped titania having surface WO_x species. The system combining the UV and near visible (up to *ca.* 500 nm) capability originated from the titania component with the visible and near infrared (up to *ca.* 1000 nm) capability of surface tungsten oxide entities.

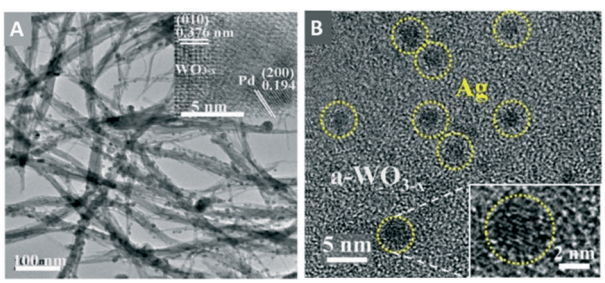

Fig. 4 A) TEM and HRTEM images of 2 wt% Pd-loaded WO_{3-x} nanowires. B) HRTEM images of Ag/a-WO_{3-x} heterostructures. A) Reprinted with permission from ref. 48 (copyright® Elsevier 2016). B) Reprinted with permission from ref. 49 (copyright® Elsevier 2019).

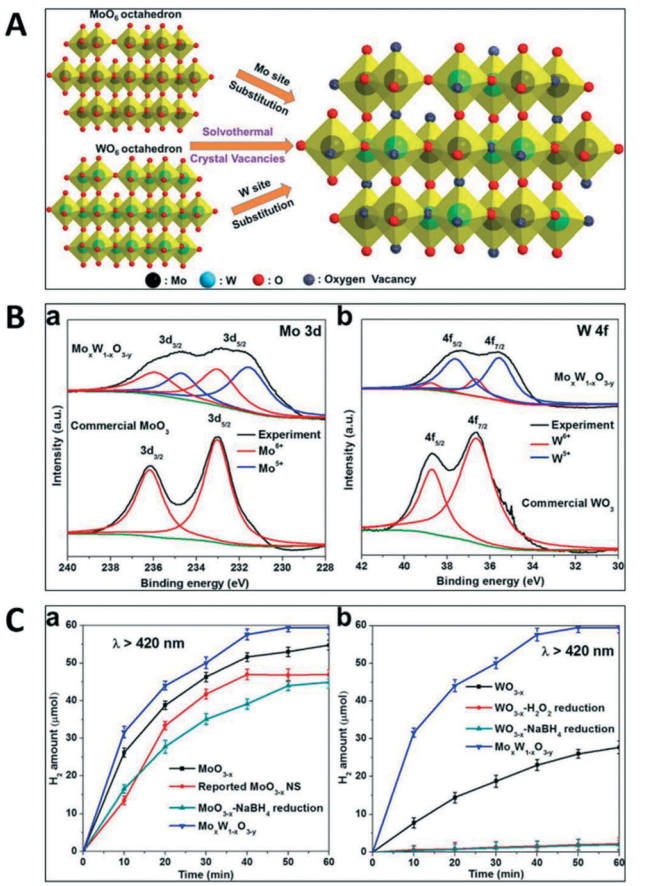

Fig. 5 A) Scheme of the plasmonic $Mo_xW_{1-x}O_{3-y}$ formation process. B) Mo 3d (a) and W 4f (b) XPS spectra of the as-prepared $Mo_xW_{1-x}O_{3-y}$ comparing with commercial oxides: MoO_3 and WO_3. C) H_2 evolution using $Mo_xW_{1-x}O_{3-y}$ and MoO_{3-x} (a), and WO_{3-x} (b) reference materials under vis-light irradiation. Reprinted with permission from ref. 57 (copyright® ACS 2017).

The high activity in the UV and near visible region was ascribed to the light absorption and handling capabilities of the doping-modified titania, presenting a reduced band gap energy with respect to the pure oxide and an efficient charge recombination. Low-energy visible and infrared photons were utilized through the plasmonic phenomenon associated to the surface W-containing species, leading in this way to a full spectrum photocatalyst with the efficient handling of concomitant thermal effects.[60] Other explored systems combined WO_{3-x} with TiO_2 to photodegrade methylene blue using full-spectrum light.[52] The combination of WO_3 with other plasmonic oxide such as MoO_3 (described below) is also an interesting strategy. The resulting mixed-cation oxide $Mo_xW_{1-x}O_{3-y}$ system semiconductor presented strong LSPR due to the anionic vacancies (detected using a multi-edge XPS study among other techniques, Fig. 5) in the structure. As can be observed in Fig. 5, the activity results showed an increase in the H_2 production as compared to (reduced, defective) WO_{3-x} and MoO_{3-x}.[57]

The preparation of heterostructured composites having non-oxide components presents an interesting strategy for the use of plasmonic oxides in thermo-photocatalysis. Fig. 6A shows the WN–WO_3 heterostructures, with the presence of two structures corroborated by physicochemical analysis. This material was explored for the thermally-assisted CO_2/H_2O photocatalytic conversion under full solar spectrum. A combined EPR-XPS study under illumination suggested, as described in Fig. 6B, that the WN–WO_3 photogenerated electrons have migrated from WO_3 to WN, following a Z-scheme mechanism rather than a type-II heterojunction mechanism.[61] Following a similar mechanism, the interaction between the phases in a Z-scheme composite has been widely studied lately. For example, the combination of WO_3 nanosheets and carbon dots (CD) demonstrated activity in photocatalysis, thermal catalysis, and thermo-photo synergistic catalysis for cyclohexane oxidation. The mechanism of cyclohexane oxidation was described, suggesting that WO_3 and CDs were excited simultaneously after irradiation with full solar spectra light. After light excitation, the electrons on the CB of WO_3 can be transferred to the CDs and annihilated at the heterointerface with holes on the VB of CDs. This mechanism enhanced the lifetime of the photoelectrons on the CB of the CDs to generate O_2-type radical species. This radical species is considered to be the main reactive species for cyclohexane oxidation (Fig. 6C).[62]

Likewise, $W_{18}O_{49}$/carbon heterostructures (Fig. 7A illustrates the preparation procedure and main morphological/structural characteristics) presented a

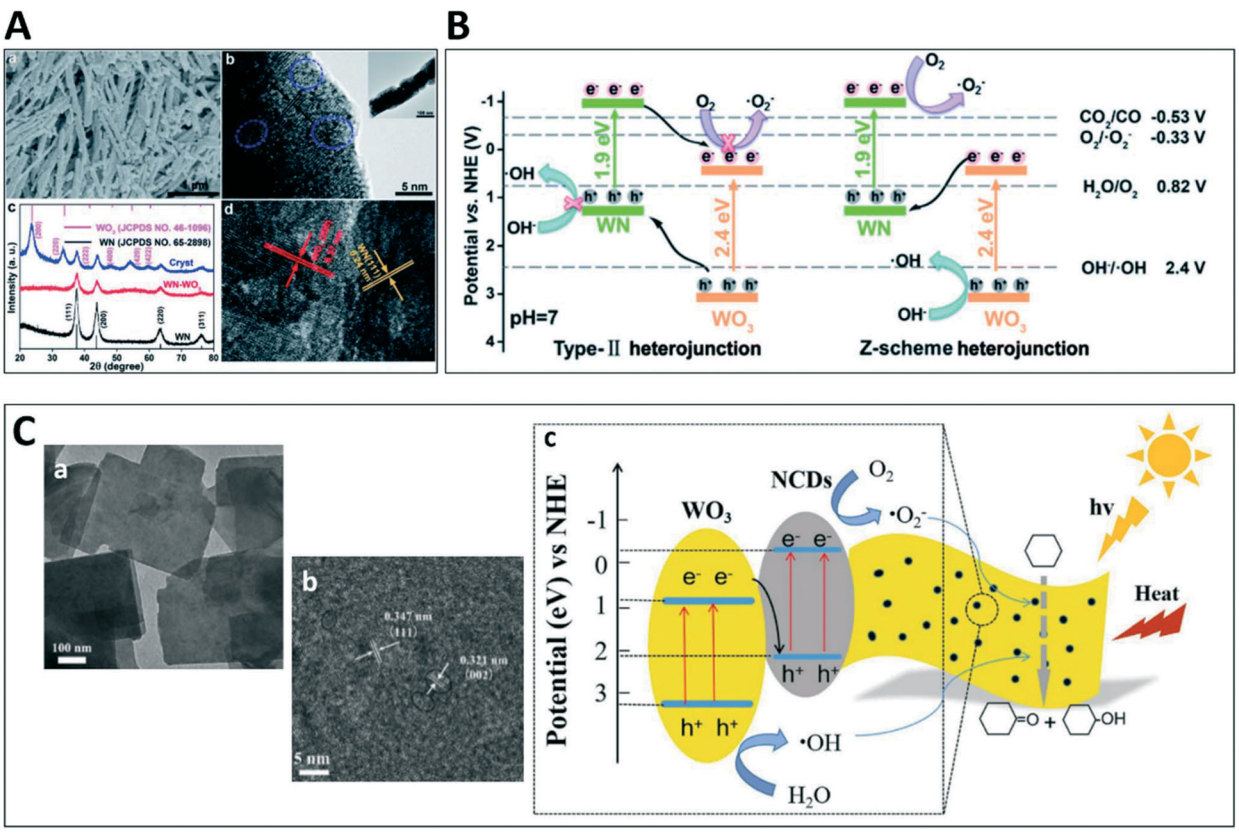

Fig. 6 A) WN–WO_3 composites characterization: SEM (a), HRTEM (inset: TEM) (b) images, XRD patterns of WN (black), WN–WO_3 (red), and well crystallized WN–WO_3 (blue) (c); HRTEM image of WN–WO_3 (d). B) Chart displaying the charge carrier species migration under type-II and Z-scheme heterojunction. C) TEM images of WO_3 nanosheets (a), WO_3-NCDs composites (b), diagram of thermo-photocatalytic cyclohexane oxidation under solar light irradiation (c). A and B) Reprinted with permission from ref. 61 (copyright® RSC 2020). C) Reprinted with permission from ref. 62 (copyright® Elsevier 2019).

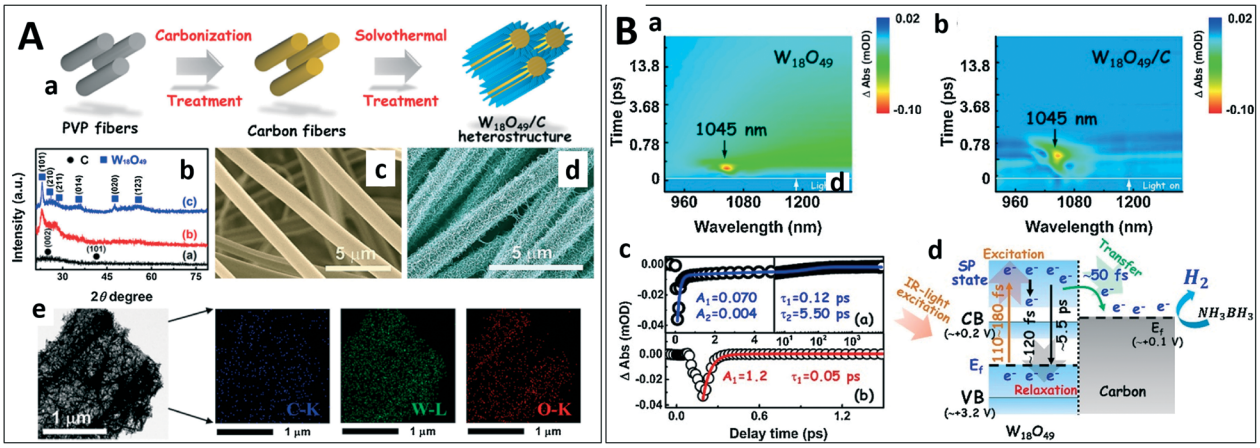

Fig. 7 A) Fabrication process scheme of the carbon fibers coated with $W_{18}O_{49}$ to prepare the material $W_{18}O_{49}$/C composite (a); XRD patterns of the carbon fibers (a-black), $W_{18}O_{49}$/C composite (b-red), $W_{18}O_{49}$ nanowires (c-blue) (b); coloured SEM images of the carbon fibers (c) and $W_{18}O_{49}$/C composite (d); TEM and C, W, and O elemental mapping images for the $W_{18}O_{49}$/C composite aggregate (e). B) Ultrafast transient absorption (TA) spectra of the $W_{18}O_{49}$ nanowires (a) and the $W_{18}O_{49}$/composite (b) after 800 nm excitation; TA kinetics curves of the $W_{18}O_{49}$ nanowires (a-top-blue) and the $W_{18}O_{49}$/C composite (b-bottom-red) excited at 1045 nm (c); kinetics process of plasmon-induced charge carrier species in the $W_{18}O_{49}$/C composite for the generation of H_2 production from NH_3BH_3 (d). Reprinted with permission from ref. 63 (copyright® Elsevier 2018).

significant increase (compared to $W_{18}O_{49}$ nanowires) for catalytic H_2 production from NH_3BH_3. Fig. 7B shows the relevant experimental data (transient absorption), supporting a complex mechanism for the reaction. The data revealed that the LSPR excitation of $W_{18}O_{49}$ in the $W_{18}O_{49}$/C heterostructure leads to the transport of hot electrons from the $W_{18}O_{49}$ nanowires to the carbon fibers within a very short timescale upon irradiation using low-energy IR photons. These electrons are involved in H_2 production (Fig. 7B).[63] The $W_{18}O_{49}$/g-C_3N_4 heterostructure has been explored for other applications such as N_2 photofixation or H_2 production.[64,65] Also, the hierarchical assembly of the $W_{18}O_{49}$ nanograsses onto the 2D g-C_3N_4 nanosheets surface have been studied. The catalytic properties relay on a Z-scheme charge-carrier separation, presenting a synergistic effect with plasmon-induced hot electrons originated at $W_{18}O_{49}$ to produce H_2. Therefore, the heterostructure promoted H_2 evolution if compared with the components separately.[55] For the same reaction, $NaYF_4$:Yb–Er/$W_{18}O_{49}$ films have been prepared to increase the upconversion luminescence of Ln^{3+}-doped $NaYF_4$ NPs. The heterostructure increases the production of H_2 (with respect to the parent systems) using the NIR-plasmonic energy upconversion process.[66] Yan *et al.* designed a Bi_4TaO_8Cl/$W_{18}O_{49}$ (BiW) system, which is assembled from Bi_4TaO_8Cl nanosheets and $W_{18}O_{49}$-nanosized particles. Under (solar-type) full spectra illumination, the study suggests that thermo-photoenergy can promote the classical (photo-type) Z-scheme charge separation behavior, providing an interesting approach to render thermo-photocatalytic systems for the reduction of CO_2.[56]

MoO_{3-x}-Based systems

MoO_{3-x} has high potential as the thermo-photocatalyst due to its redox properties as well as low cost and non-toxicity.[67] MoO_3 is an important wide band-gap n-type semiconductor (band-gap, 3.2 eV) and has been extensively explored as a photochromic and electrochromic material, which can change its optical properties in response to external light and electric stimulus.[68] However, defect-free MoO_3 presents low photocatalytic activity.[69] Therefore, MoO_{3-x} has been engineered to create more effective systems with different purposes. Similarly to the WO_3 family, the common approach to exploit MoO_{3-x} plasmonic systems explored its combination with noble metals, with an enhanced thermo-photocatalytic activity for a range of applications such as H_2 production or deoxygenation of sulfoxides.[70,71] On the other hand, MoO_{3-x} alone has been proposed to enhance the hydrogen production. MoO_{3-x} 2D nanosheets were prepared using a solvothermal treatment in ethanol. Under visible light irradiation, the nanosheets showed a significant increase in H_2 production from ammonia borane.[38] The synthetic parameters, such as temperature and type of reacting solvents used, play an essential role in the evolution of phase and morphology of the nanostructures, having high influence in the LSPR appearing from the visible to the NIR region. Under visible light irradiation, the plasmonic MoO_{3-x} nanosheets showed enhanced light absorption and hydrogen production (Fig. 8).

Similarly, Li *et al.* have prepared a highly active plasmon thermo-photocatalyst by inducing oxygen vacancies in MoO_{3-x}. The vacancies increase the efficiency of CO_2 reduction to CO and CH_4 by capturing the NIR photons, boosting the yield of these products compared to pure MoO_3.[69] Surface analysis and theoretical calculations were performed. Based on the results of the characterization, the authors suggested that the barrier for CO_2 hydrogenation was reduced by a defect-derived electronic state, which are in turn related to the production oxygen vacancies in MoO_{3-x}. These works evidenced that thermo-photo technology based on bare

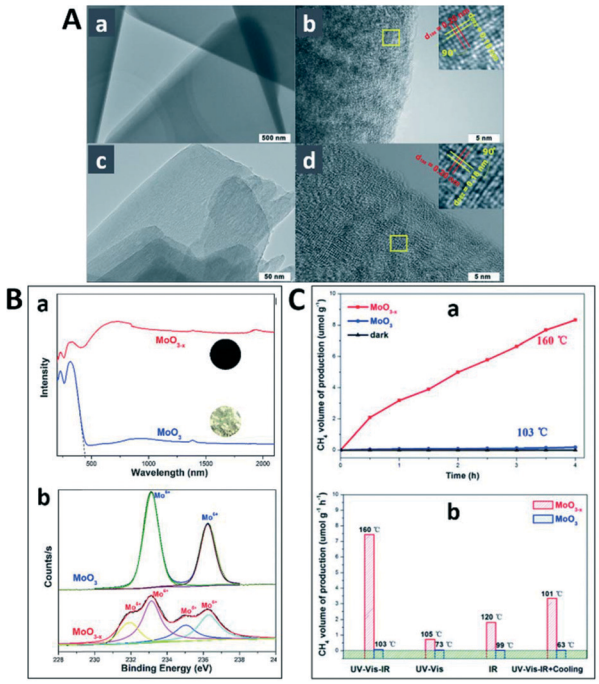

Fig. 8 Physico-chemical characterization of Mo oxide materials: A) TEM (a) and HRTEM (b) images of MoO_3, and TEM (c) and HRTEM (d) images of MoO_{3-x} catalysts; B) UV-vis-NIR diffuse reflectance spectra (a) and Mo 3d XPS spectra (b). C) CH_4 production under UV-vis-IR irradiation for 4 h (a) and CH_4 production rate over under UV-vis-IR, UV-vis, and IR light irradiation for 1 h (b) over MoO_{3-x} and MoO_3. Reprinted with permission from ref. 69 (copyright® RSC 2019).

Mo-containing oxide can be rather useful. Yet, more comprehensive studies of the action mechanism need to be carried out in order to assess the applicability of this kind of system. For the production of hydrogen, more complex Er–Yb:TiO_2/MoO_{3-x} nanocomposite materials have been used. In this system, the interface between Er–Yb:TiO_2 and MoO_{3-x} acts as a charge carrier channel to separate the plasmon-induced charge carrier species.[72]

Very recently, the MoS_2/MoO_{3-x} heterostructure was prepared by light-induced partial *in situ* oxidation of MoS_2 nanosheets. The system displays a strong LSPR effect in the vis-NIR region, which promoted the formation of hot electrons.[73] The TEM images (Fig. 9A) showed the formation of the MoS_2/MoO_{3-x} heterostructure. The synthesis allowed the oxidation of Mo atoms along the edges or at the defects of MoS_2, promoting the formation of oxygen vacancies within the surface. Fig. 9B shows a schematic mechanism of the photocatalytic reduction of CO_2. The oxygen vacancy induces a defect band (DB), located near but below the CB in MoO_{3-x}. The electrons on the CB of MoS_2, excited by visible light, are easily transferred to the DB of MoO_{3-x}, favoring the separation of the charge carrier. Under visible or NIR irradiation, free-type electrons on DB became excited (hot carrier species) and subsequently engaged in CO_2 reduction, thus promoting the activity. Under UV irradiation, electrons are directly excited to the CB of MoO_{3-x}, followed by non-radiative decay to the defect band (DB).

Based on the multi-technique study of charge handling behavior by the composite (Fig. 9B), the authors claimed that the continuous injection of UV-excited electron stabilizes free-type (or quasi-band-type) electrons in the DB sub-band while vis-NIR illumination excited the DB electrons to become hot electrons that will be transferred to the MoO_{3-x} CB, synergistically boosting CO_2 reduction under full sunlight illumination conditions.

Cu_2O-Based systems

Plasmonic activity of Cu-based oxide systems have been explored since they can exhibit LSPR absorbance at *ca.* 600 nm. Similarly, in W- and Mo-based systems, the plasmonic activity of Cu-based systems is frequently utilized by combining Cu_2O with noble metals. In this case, Au and Ag have been combined with Cu_2O structures, such as nanowires[74,75] or NPs.[29,76] As mentioned in section 1 of this review article, the facile oxidation (of Cu^0 and Cu^{1+} to Cu^{2+}) and back-reaction (reduction) taking place in air (first reaction) and/or under reaction conditions represent an important disadvantage of its use.

Very recently, Zheng *et al.* designed a single-pot strategy synthesis to synthesize a composite having a metal (Cu)/oxide semiconductor (Cu_2O) interface and tunable molar ratio of the components. Fig. 10A illustrates the composite structure. The Schottky contact formed between Cu(0) and the Cu_2O semiconductor renders an active Cu(0)/Cu_2O interface, playing a key role in promoting the catalytic reduction of CO_2 by enhancing the light absorption performance and photogenerated electron–hole separation.[77] Robatjazi *et al.* prepared a system based on the Al@Cu_2O nanoantenna-reactor, where the nanoantenna (Cu_2O) shows plasmonic behavior and Al acts as light-related heating component (Fig. 10B). The separation of the catalytic (Cu_2O) and light capture (Al) functions into different materials promotes higher quantum efficiencies in chemical conversion. The reverse water-gas shift process (rWGS) is an approach for CO_2 reduction to CO but also appears as a side reaction in CO_2 reduction to other products. Al@Cu_2O presented effective and selective rWGS under mild conventional thermal conditions with many potential industrial applications.[78] Following a similar approach, other photo-thermal catalytic devices have been designed. CO_2 methanation using water has been explored by including carbon dots (CDs) on Cu/TiO_2.[79] Under UV irradiation, this catalytic system produces CH_4 at the temperature (>150 °C). The mechanism of the reaction was studied by *in situ* DRIFTS (diffuse reflectance IR Fourier transform spectroscopy). The study indicates that the CO_2 methanation process over CD-Cu/TiO_2 can be mainly considered as two different processes. First, CO_2 is reduced to CO by Cu(I) (Cu_2O) ($CO_2 + Cu_2O \rightarrow CO + CuO$), and second, CO is reduced to CH_4 by H_2O. In this case, the carbon dots have a dual function; they act as an electron storage center and could also capture UV light-generated holes from titania. Critically, a Cu(I)/Cu(II) cycle can take place with concomitant

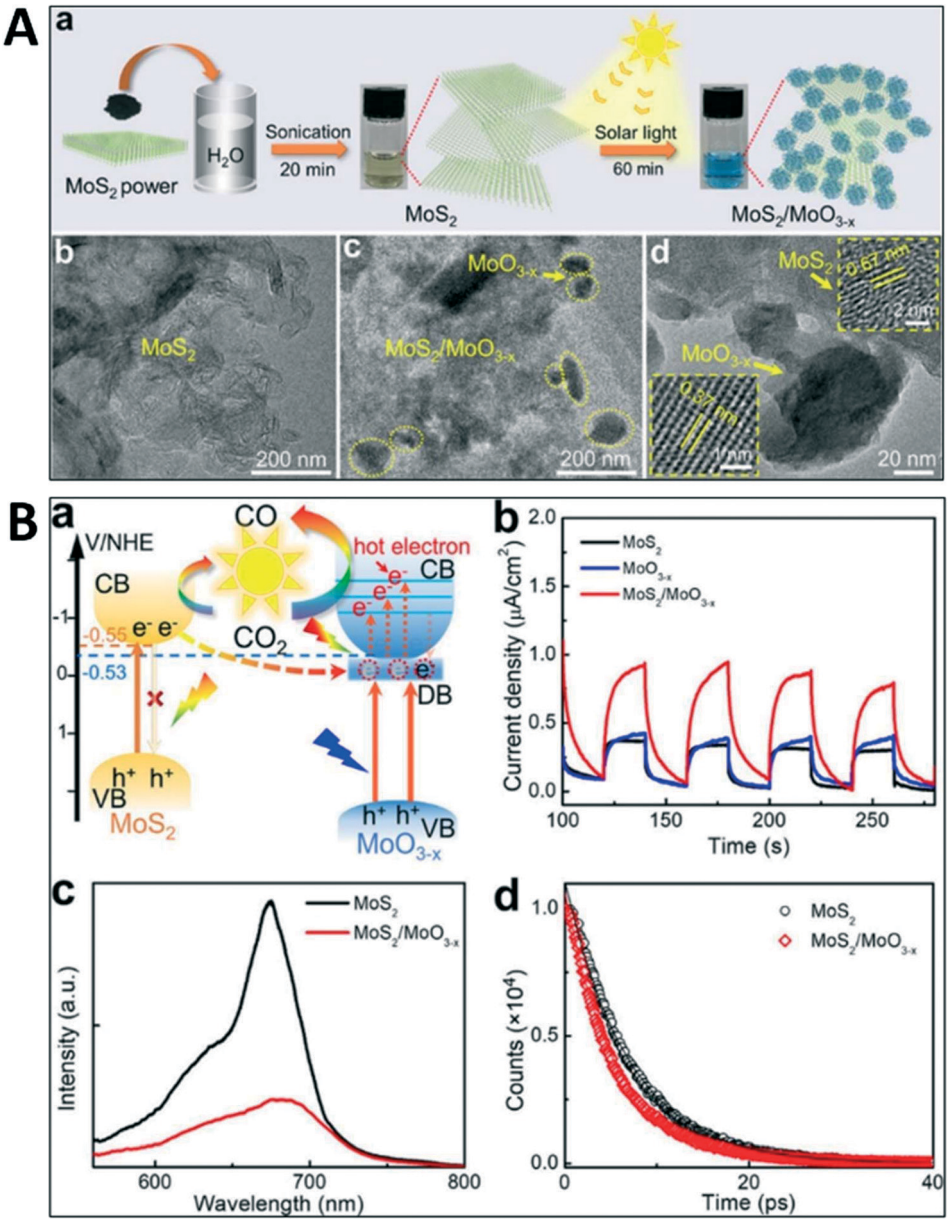

Fig. 9 A) Illustration of the plasmonic MoS_2/MoO_{3-x} composite synthesized *via* light-induced *in situ* oxidation of MoS_2 nanosheets (a); TEM image of MoS_2 material (b); TEM (c) and HRTEM (d) images of the MoS_2/MoO_{3-x} composite. B) Excitation and charge transfer of the MoS_2/MoO_{3-x} composite (a); MoS_2, MoO_{3-x}, and MoS_2/MoO_{3-x} photocurrent responses (b); PL spectra (c); and decay curves (d) of MoS_2/MoO_{3-x} (red) and MoS_2 (black) materials. Reprinted with permission from ref. 73 (copyright® ACS 2019).

electron storage and release, with a the principal role of CDs as the electron handling component and the stabilizer of the redox state of copper, limiting over-reduction at a high temperature (Fig. 10C).[79] On the other hand, Cu_2O combined with graphene oxide (GO) was prepared by the chemical reduction of $Cu(NO_3)_2$ in the presence of GO precursors under Ar atmosphere, obtaining homogeneously dispersed Cu_2O NPs on the catalyst surface (Fig. 10D). The Cu_2O/GO system presented a highly specific CH_4 formation rate and quantum yield at temperatures below the typical Sabatier ($CO_2 + 4H_2 \rightarrow CH_4 + 2H_2O$) reaction temperature (>350 °C). The catalytic action was explained as a synergistic effect between G and the Cu_2O NPs, with promoted charge separation by facilitating the migration of the conduction band electrons generated in Cu_2O to GO. Photo-induced electron transfer from the Cu_2O/GO photocatalyst to CO_2 takes place at the same time that light-induced local temperature appears to facilitate H_2 activation. In addition, heating accelerates H_2O desorption, improving the overall CH_4 formation.[80] Recently, the Cu@Cu_2O/ZnO nanostructure has been synthesized to enhance the photocatalytic H_2 production.[81] The presence of Cu@Cu_2O significantly increased the production of H_2 compared to pure ZnO. Excited with UV-visible light, hot electrons are generated at the Cu component, which moved into the CB of Cu_2O and were subsequently injected into the CB of ZnO. This process

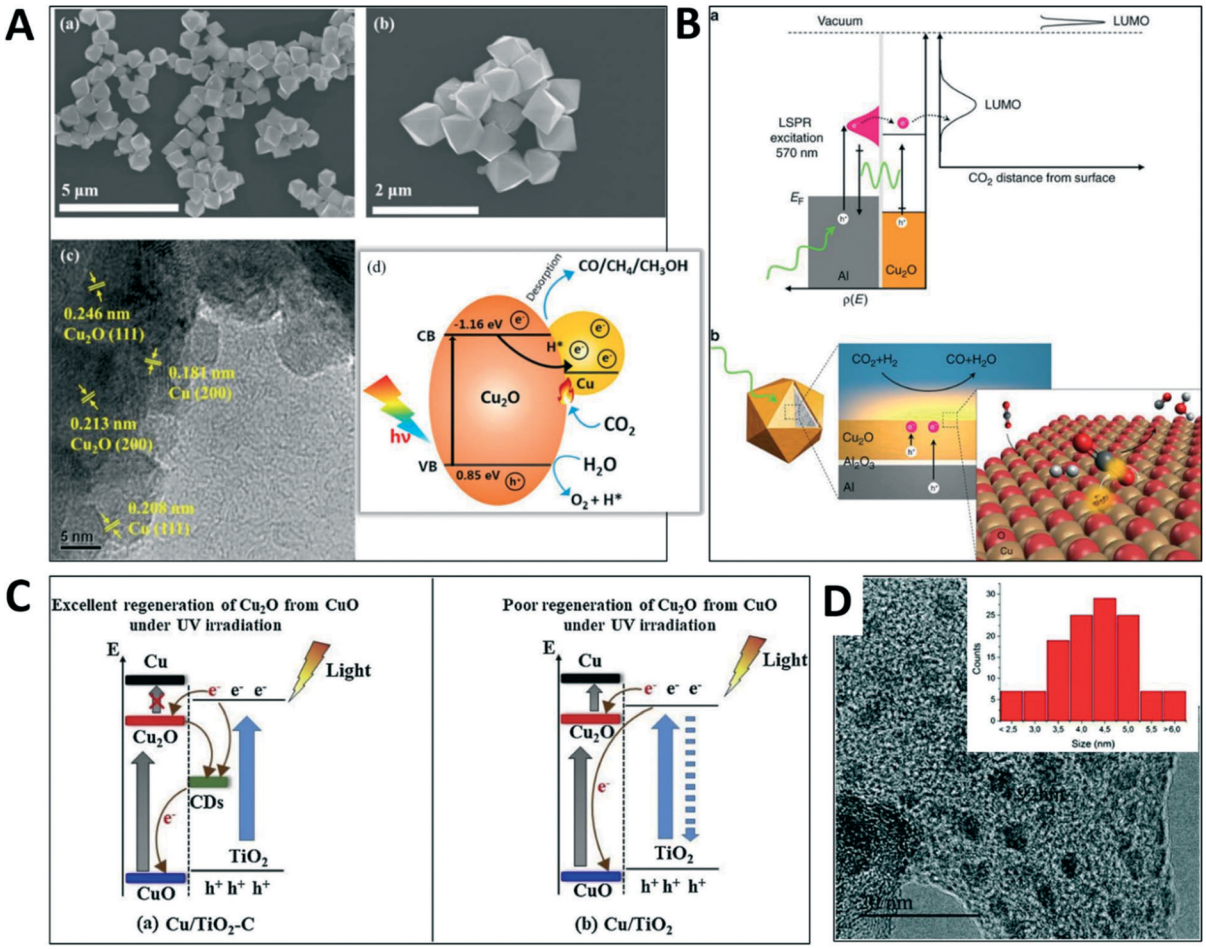

Fig. 10 A) SEM (a and b) and HRTEM (c) images of a Cu_2O plasmonic system with the schematic representation of the thermo-photocatalytic mechanism (d). B) Energy band diagram of Al@Cu_2O for the carrier generation induced by plasmon (a) and scheme of plasmon-induced carrier-assisted rWGS process (b). C) Charge carrier handling scheme taking place under UV illumination in Cu/TiO_2-C (a) and Cu/TiO_2 (b) systems. D) HRTEM image of Cu_2O/G and particle size distribution of Cu_2O NP. A) Reprinted with permission from ref. 77 (copyright® ACS 2021). B) Reprinted with permission from ref. 78 (copyright® Springer Nature 2017). C) Reprinted with permission from ref. 79 (copyright® Elsevier 2019). D) Reprinted with permission from ref. 80 (copyright® RSC 2017).

is synergistically improved by the photoactivity of ZnO, which presents holes in the VB after irradiation, which are transferred to the VB of Cu_2O. The result is efficient light absorption and charge separation under broadband (sunlight-type) illumination, inducing H_2 production in the interphase.[81]

3. Defective oxides

The chemistry and engineering of defects in metal oxides have become of great interest because they can have a key effect on the catalytic activity of metal oxide systems. As depicted in Fig. 2B, many defects are detected in oxide systems. This makes it complex to render general ideas about their catalytic role. In spite of this, the defect chemistry appears critical in thermal catalysis by several reasons including the presence of surface defects, facilitating the adsorption and activation of the reactants as well as anion mobility in order the provide the active species in specific mechanisms such as Mars–van Krevelen and others.[1,82] Similarly, in the light-driven reactions, they can play the above-mentioned roles but are also critical actors in charge capture and recombination taking place after light excitation. For example, in titania–anatase, radiative recombination always occurs with the participation of a defect-related trapped species.[83] The interplay between all these possible roles of the defects depicts a complex scenario that is rather useful in the context of thermo-photocatalysis. Herein, we analyzed several composite systems containing Co_3O_4, CeO_2, MnO_2, BiO_2, or In_2O_3 oxides among others as the key components of the systems. They represent the examples of oxides where the defect-related features control or strongly affect the catalytic behavior.

CoO_x-Based systems

Co_3O_4, with a significant number of oxygen vacancy defects present in the so-called reduced Co_3O_4, is a typical example.[84]

The catalytic activity of this type of compound has been explained based on the oxygen vacancies on the surface of the material. Specifically, DFT calculations have been carried out to determine the influence of the structure on the catalyst activity. A new state, located within the band gap and below the conduction band minimum, has been identified for reduced Co_3O_4. The work indicated that when the two electrons (associated with the presence of an anion lattice vacancy) are excited, the Fermi level appears near the conduction band edge and the energy of the Vo^{2+} formation is *ca.* 1 eV lower than that in similar materials, such as TiO_2-rutile. The concentration of the oxygen vacancies can be determined by the following equation

$$n = N \exp\left(-\frac{E_{vf}}{k_B T}\right)$$

where, N is the number of possible lattice site per volume unit necessary to form the defect, k_B is the Boltzmann's constant, and T is the temperature. Therefore, the lower formation energy means more oxygen vacancies and greater oxygen release capacity. Fig. 11A shows the distribution of the two electrons associated with the anion vacancy. According to the authors' discussion, the removal of an oxygen atom causes the two electrons occupying the 2p orbitals of oxygen to delocalize around the three neighboring atoms of Co^{3+} and O. This causes further electron delocalization in reduced Co_3O_4. Therefore, the oxygen vacancies present in the structure of Co_3O_4 can increase the number of active sites on the surface/subsurface with redox capability. Moreover, the delocalized electrons related to oxygen vacancies increase the conductivity of Co_3O_4. The combination of all these factors promotes the catalytic behavior of Co_3O_4.

Several articles scrutinized the thermo-photocatalytic activity of the Co_3O_4-based systems.[85,86] An example is the article published by Lan *et al.*[85] The Co_3O_4 mesoporous nanorods system (Co_3O_4-MNR) with Co^{2+} vacancies (instead of the anion vacancies explored at the bulk oxide, ref. 84) has been synthesized. This sample was tested for the benzene gas-phase oxidation process and it was compared with the commercial Co_3O_4 oxide (with less defects) and the TiO_2 (P25) material. Co_3O_4-MNR has shown higher thermo-photocatalytic activity than Co_3O_4. The EPR and XPS results indicated that the Co^{2+}/Co^{3+} ratio for Co_3O_4-MNR was 1 : 3.17, which is lower than that of bulk-type Co_3O_4 (1 : 2). In order to determine the mechanism of the reaction, Co_3O_4-MNR was tested under UV-vis-IR illumination at room temperature, and no catalytic activity was shown. The absence of photocatalytic activity was attributed to the fact that the photogenerated holes (located at the VB) do not have enough potential to oxidize hydroxyl groups and, consequently, recalcitrant benzene. Therefore, the very high thermo-photocatalytic activity of Co_3O_4-MNR under illumination comes from a sunlight-driven thermo-catalytic oxidation mechanism. In Fig. 11B, a scheme of the proposed mechanism is presented. In the first place, the authors have attributed the increase in the catalytic activity to the strong light absorption of Co_3O_4-MNR, which originated the concomitant effect on the surface temperature (by multiple de-excitation channels for charge carrier species and phonons of the solid) to trigger conversion. The results obtained suggest that the Co_3O_4-MNR system can convert UV-vis-IR and vis-IR light into thermal energy efficiently. Furthermore, the DFT calculations were performed in order to study the effect of Co^{2+} vacancy defects on the lattice oxygen activity in the Co_3O_4 system. The results indicated that the presence of Co^{2+} vacancy on the surface promotes

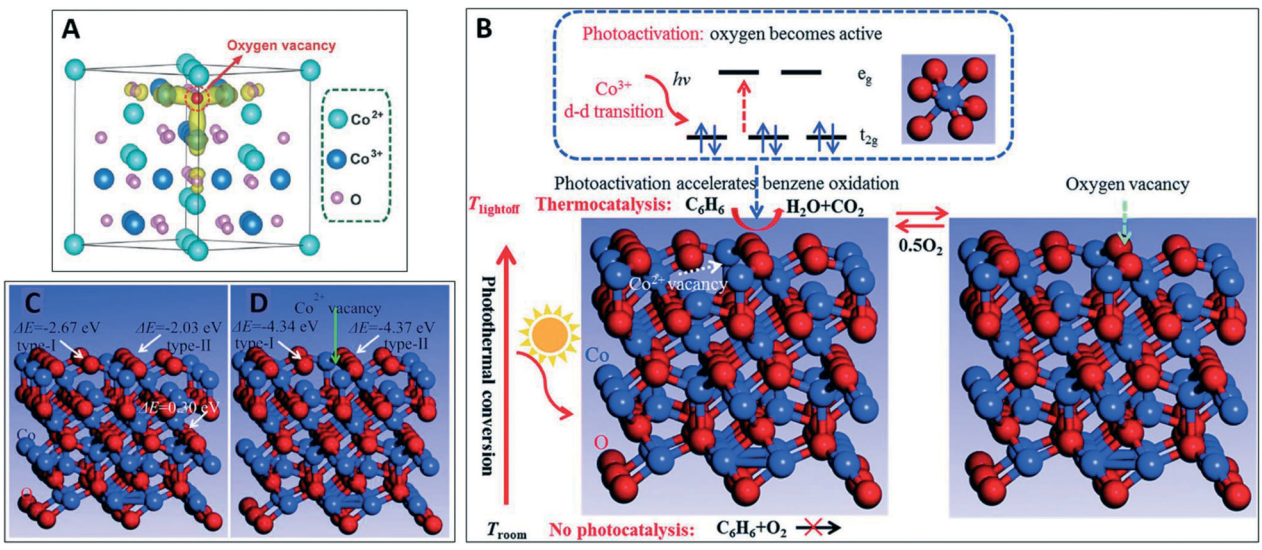

Fig. 11 A) The reduced Co_3O_4 partial charge density. B) Schematic representation of the photoactivation under solar light irradiation and thermocatalysis on Co_3O_4 with Co^{2+} vacancy defects. The calculated slabs of $Co_{48}O_{64}$ with no Co^{2+} vacancy (C) and with one Co^{2+} vacancy (D). A) Reprinted with permission from ref. 84 (copyright® Wiley 2014). B–D) Reprinted with permission from ref. 85 (copyright® Wiley 2018).

the activity of the surface lattice oxygen. As shown in Fig. 11C and D, the energy for removing one oxygen atom from the surface by CO was calculated. The removal of a single oxygen atom on the Co_3O_4 slabs without a Co^{2+} vacancy is always disfavored (two oxygen positions tested) with respect to the Co_3O_4 slabs with one Co^{2+} vacancy. In addition, the energy for removing one oxygen atom in the bulk is much higher than that on the surface, favoring their presence at the surface sites that are able to interact with the reactants.

Ultrathin mesoporous Co_3O_4 nanosheets on stainless steel mesh (SS-Co_3O_4) were utilized by Zheng *et al.* for VOC oxidation.[86] The thermo-photocatalytic activity was tested for the aerobic oxidation of C_3H_6 and C_3H_8 under simulated sunlight and it was compared with the activity of P25, TiO_2, and bulk-type Co_3O_4. The results showed that the novel SS-Co_3O_4 exhibits superior activity with respect to all the reference systems mentioned. The authors related this fact to the heating effect, a result of the strong absorption of the solar spectrum, which caused an important increase in the temperature above the light-off temperature, facilitating VOCs oxidation. Moreover, the SS-Co_3O_4 properties such as supported metal, porous foam-like interior architecture and the ultra-thin two-dimensional shape could lead to certain advantages. They are probably related to the beneficial utilization of the photo-to-thermal conversion, increasing the number of catalytically active sites, and also enhancing the mobility and amount of surface lattice oxygen species, ending in the excellent thermo-photocatalytic activity displayed by SS-Co_3O_4.

Different Co_3O_4-based composites have been studied.[87–91] Shi *et al.* studied the TiO_2/Co_3O_4 nanocomposite synthesized to improve the thermo-photocatalytic activity.[87] For this propose, different Co/Ti molar ratios have been prepared and tested for gas-phase benzene degradation under UV-vis-IR irradiation. The thermo-photocatalytic activities of the composites were compared with TiO_2 (P25). The composites exhibited higher thermo-photocatalytic activity than the reference, highlighting the composite with a 0.30 molar ratio. This sample degraded 95% of benzene within 40 min. The results showed that TiO_2/Co_3O_4 exhibits photocatalytic activity but much lower than that of its thermo-photo counterpart. Therefore, the strong thermo-photocatalytic activity would be driven by light-triggered thermocatalytic benzene oxidation on Co_3O_4. Fig. 12A illustrates the photo and light-driven steps of the thermo-photo processes. The strong optical absorption of the composite causes the raising of the surface temperature due to photo-to-thermal conversion. The authors suggest that to promote the beneficial effect between light and thermal energy on Co_3O_4 and TiO_2, there must be an effective migration of the light-triggered active species at the interface between the oxide components. To determine whether this occurs, the authors prepared a physical mixture of nano Co_3O_4 and TiO_2 (P25). The results showed that the thermo-photocatalytic activity in the physical mixture was lower than that of the composite formed by the same Co/Ti molar ratio. Therefore, the efficient migration of the photogenerated active species through the interface of components plays a key role in the thermo-photo synergistic effect. Based on the results obtained, the authors proposed the following mechanism. On the one hand, the electrons are excited from the TiO_2 valence band to its conduction band by absorbing UV radiation. The electrons reduced adsorbed O_2 molecules on

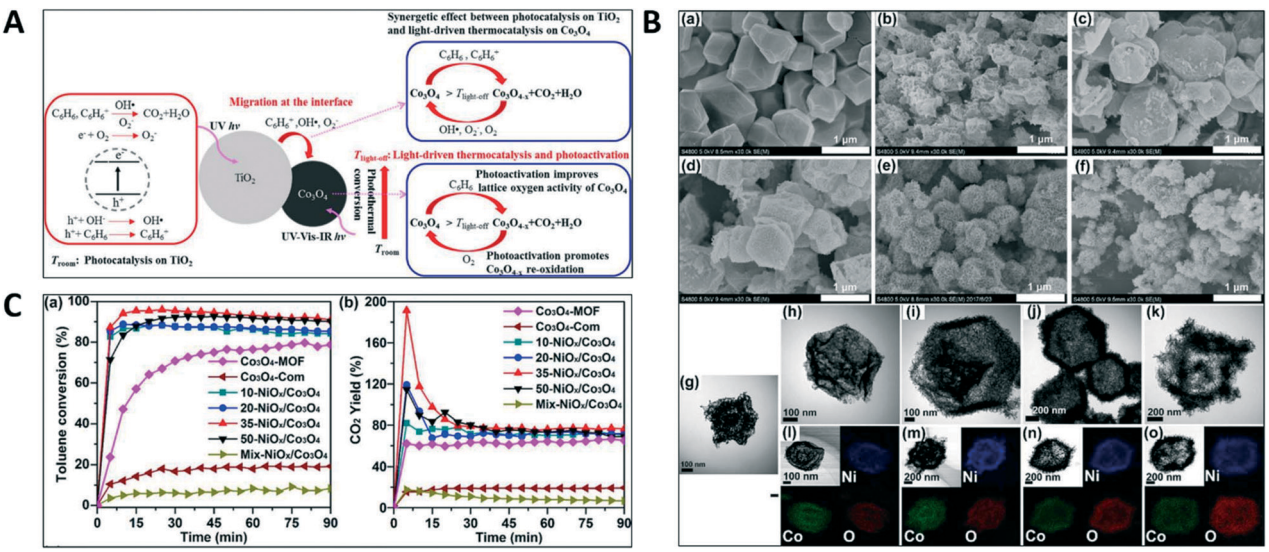

Fig. 12 A) Schematic representation of photocatalysis (TiO_2), light-driven thermocatalysis, and photoactivation (Co_3O_4), and the synergistic effect between light-driven thermocatalysis (Co_3O_4) and UV-photocatalysis (TiO_2). B) SEM images: ZIF-67 (a), Co_3O_4-MOF (b), 10-NiO_x/Co_3O_4 (c), 20-NiO_x/Co_3O_4 (d), 35-NiO_x/Co_3O_4 (e), 50-NiO_x/Co_3O_4 (f); TEM images: Co_3O_4-MOF (g), 10-NiO_x/Co_3O_4 (h), 20-NiO_x/Co_3O_4 (i), 35-NiO_x/Co_3O_4 (j), 50-NiO_x/Co_3O_4 (k); TEM element mapping images of 10-NiO_x/Co_3O_4 (l), 20-NiO_x/Co_3O_4 (m), 35-NiO_x/Co_3O_4 (n), 50-NiO_x/Co_3O_4 (o). C) Toluene (gas) degradation under simulated sun-light irradiation over different catalysts (a and b). A) Reprinted with permission from ref. 87 (copyright® ACS 2018). B and C) Reprinted with permission from ref. 88 (copyright® ACS 2018).

TiO_2, generating the active O_2^- species. The holes oxidized the hydroxyl and benzene adsorbed species on TiO_2 to form $OH^•$ and $C_6H_6^+$ radicals. These photogenerated active species can likely migrate through the Co_3O_4/TiO_2 interface to the Co_3O_4 component. On the other hand, light-promoted thermocatalytic benzene degradation on nano Co_3O_4 proceeds upon UV-vis-IR irradiation. Thermocatalytic oxidation in Co_3O_4 takes place through a Mars–van Krevelen redox mechanism (lattice oxygen species oxidizes C_6H_6, and O_2 subsequently reoxidizes reduced cobalt oxide sites). Due to the fact that the photogenerated $C_6H_6^+$ species are more active than the non-charged (neutral) molecule,[92] the reduction of the surface Co_3O_4 entities by benzene is promoted. Similar to the high activity of O_2^- species and OH radicals,[92] Co_3O_4 reoxidation is strongly favored. All these phenomena work cooperatively and accelerated light-promoted thermocatalytic benzene oxidation with significant effect on the reaction rate.

A series of hollow NiO_x/Co_3O_4 composites have been synthesized by Chen *et al.* and were tested for toluene oxidation.[88] Hollow NiO_x/Co_3O_4 compounds derived from ZIF-67 were synthesized by the impregnation method. Fig. 12B encloses a microscopy study of the structural and morphological properties of the samples. As can be seen, the ZIF-67 precursors trigger the presence of a polyhedric-type structure after calcination. The resulting sample (called Co_3O_4-MOF) exhibits some kind of shrinking morphology originated by the agglomeration of the Co_3O_4 nanocrystallites. When Ni is added to the catalyst formulation, the evolution of the external shells of the particle was clearly observed. The TEM-EDS images confirmed the formation of a core–shell type morphology with an NiO_x shell and a Co_3O_4 core. In addition, light-driven catalytic activity under simulated sunlight was studied. Fig. 12C shows the degradation of toluene under the irradiation of simulated sunlight. The composites exhibit enhanced catalytic activity with respect to pure Co_3O_4-MOF, commercial Co_3O_4, and the mechanical mixture of NiO_x and Co_3O_4 (this one presents the lowest catalytic activity). It is to be noted that the 35-NiO_x/Co_3O_4 catalyst (35 wt% of NiO_x) showed the best toluene conversion. The authors determined that the strong metal oxide interaction, catalyst structure, and appropriate Ni content are crucial factors to improve the catalytic activity of the catalyst. The optimum activity for the 35-NiO_x/Co_3O_4 sample is connected with the highest light absorption, which is in turn related with the homogeneous distribution of Ni/Co and a close contact of NiO_x and Co_3O_4 on the shells. The authors studied the low-temperature regime under light irradiation. The absence of activity was observed; therefore, the process is not carried out by traditional photocatalysis. The studied concluded that absorbed light is efficiently converted into heat through non-radiative recombination, contributing to the increase in the temperature at the macroscopic scale.

Another example of composites formed by Co_3O_4 was published by Lou *et al.*[89] Fe_3Si-Assisted Co_3O_4 nanorods were synthesized for CO oxidation. The catalytic reduction of CO occurs at high temperatures; however, the authors of this article demonstrated that the composites formed by Fe_3Si/Co_3O_4 are able to convert light into heat to drive the oxidation of CO. Surface decoration or doping are other strategies that have been used to promote the catalytic activity. Zhao *et al.* published an article where the synthesized porous Co_3O_4 nanosheets were decorated with Cu^{2+}.[93] The reported results show that this type of composite has a reaction rate that is 1.76 times higher than that of Co_3O_4 for the thermo-photo oxidation of toluene. In fact, the process shows a solar light-driven thermo-catalytic reaction. Finally, an ACo_2O_4 type spinel was synthesized by Chen *et al.* for photo-promoted thermo-catalytic removal of VOCs.[94] Different spinels have been synthesized with A = Ni, Cu, Fe, and Mn. All the spinel systems showed significant light absorption over the hole solar spectrum and associated heating effects, rendering sufficient thermal energy to promote the catalytic degradation of toluene. However, the catalyst displaying the highest thermo-photocatalytic activity for the target molecule oxidation process was Ni. The authors explained this excellent light-driven catalytic performance mainly by the strong light absorption, high photothermal conversion, increasing active oxygen species, and larger surface area.

MnO_x-Based systems

Another different type of material widely studied in thermo-photocatalytic processes corresponds to manganese oxide. MnO_2 can display different phases (polymorphs) depending on the synthesis method.[95] Fig. 13 shows different polymorphs of MnO_2. All of them differ by the different manner of interlacing the chains of the octahedral [MnO_6] units. The Mn atom occupies the center of the eight-surface body and the oxygen is on the top of the eight-surface body angle.

The romanechite δ-MnO_2 phase (Fig. 13A–D) displays a hierarchical layer with edge-sharing [MnO_6] octahedra sheets. The hollandite α-MnO_2 structure is built with the double-chain of edge-sharing octahedral units [MnO_6] with two types of channels (1 × 1 and 2 × 2) extending along the *c*-axis (Fig. 13E–H). The pyrolusite β-MnO_2 phase shows a rutile-type structure. In this case, the strings of edge-sharing octahedra extended along the *c*-axis are formed by [MnO_6] units. Then, by sharing the common corner, they connect with nearby chains forming a (1 × 1) tunnel (Fig. 13I–L). The different crystal structures lead to different channel diameter, with the magnitude of δ-MnO_2 being larger than that of α-MnO_2 and β-MnO_2. Thus, the different structures modify the material properties and hence the catalytic properties of the material.

Several articles have been published where "reduced" manganese oxide (MnO_x) has been synthesized pure,[96] or in composite systems with metals[97–100] or other oxides.[101–106] Yang *et al.* published an article reporting the synthesis of

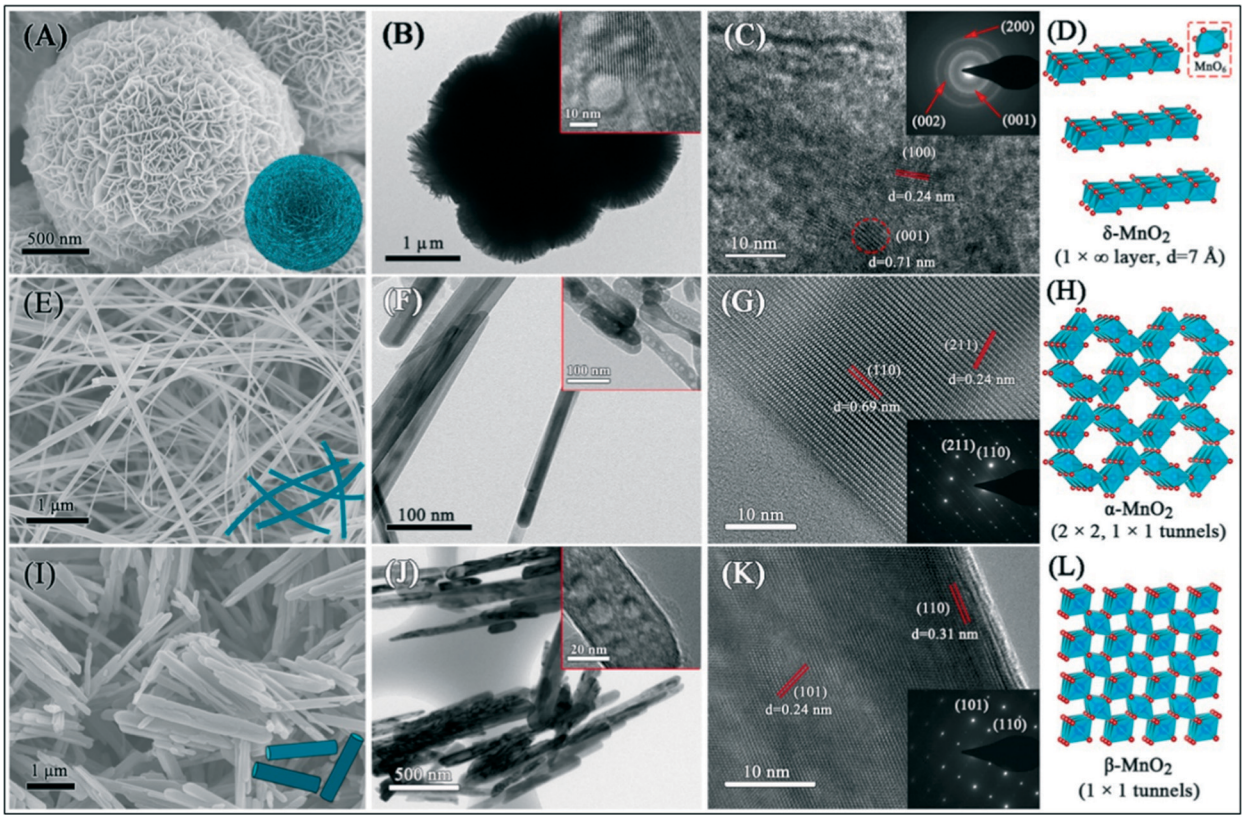

Fig. 13 SEM images (A, E and I); HRTEM images (B, F and J); SAED pattern (insets C, G and K); and crystal structure diagrams (D, H and L) of MnO_2 catalysts: (A–D) δ-MnO_2, (E–H) α-MnO_2, and (I–L) β-MnO_2. Reprinted with permission from ref. 95 (copyright® Elsevier 2021).

ramsdellite (gamma) MnO_2 hollow spheres (Fig. 14A and B) composed by closely stacked nanosheets (R-MnO_2-HS).[96] R-MnO_2-HS was evaluated in thermo-photocatalysis for benzene oxidation under Xe lamp irradiation. The results show dramatic superior activity with respect to TiO_2 (P25). The authors reported that this type of oxide produced the rapid diminishing of benzene concentration, accompanied by a fast increase in the CO_2 concentration. After 30 min of irradiation, benzene is almost completely oxidized.

In addition, the thermo-photo benzene catalytic oxidation taking place under the visible-infrared (visible-IR) or infrared (IR) irradiation was evaluated and the results demonstrated that R-MnO_2-HS shows high catalytic activity under all the mentioned illumination conditions. The process again triggers the surface temperature to raise activity through a thermo-photo conversion process, taking place after light absorption. To clarify the mechanism, the bare photocatalytic activity of R-MnO_2-HS at room temperature under full-spectrum solar irradiation was tested. The results show lack of CO_2 production, pointing out that conventional photocatalysis does not occur on R-MnO_2-HS. When the temperature is above $T_{light\text{-}off}$, the thermocatalytic degradation of benzene takes place. The oxidation of the organic molecules species is carried out by surface lattice oxygen of the manganese oxide, which are subsequently annihilated by O_2 molecules (Mars–van Krevelen mechanism).[107] Finally, DFT calculations (results summarized in Fig. 14C and D) were carried out. The authors reported that the energy (ΔE) for removing one oxygen from the $Mn_{32}O_{64}$ supercell in the excited state was 1.36 eV, which was lower than the ΔE in the ground state (2.05 eV). These theoretical results indicate that the lattice oxygen activity of the ramsdellite MnO_2 sample could be increased by solar light irradiation. This adds a beneficial (catalytic) effect to

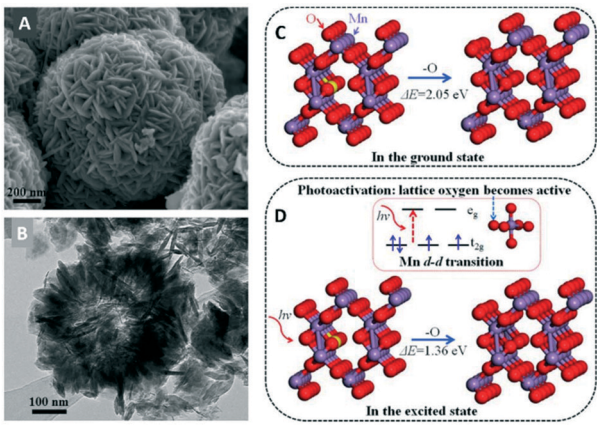

Fig. 14 SEM (A) and TEM (B) micrographs of the R-MnO_2-HS sample. Calculated supercell of ramsdellite MnO_2 ($Mn_{32}O_{64}$) and the corresponding energy of removing one oxygen (yellow sphere) in the ground (C) and excited (D) states. Reprinted with permission from ref. 96 (copyright® ACS 2017).

the already mentioned surface temperature effects. Also, for the thermo-photo degradation of VOCs, in this case, benzene as the target molecule, an amorphous manganese iron oxide (called Mn_xFeO_y-70) has been designed. The increased catalytic activity was ascribed to the higher lattice oxygen activity, which is essential for benzene oxidation under UV-vis-IR irradiation. In addition, the system showed excellent thermo-photocatalytic durability, presenting stable long-term operation under the reaction.[98] Other Mn-containing structured nanoflowers, with an octahedral layered birnessite structure, showed thermo-photo activity based on the enhanced activity of the described lattice oxygen. The material showed high efficiency for CO oxidation under full-spectrum solar, visible-infrared, as well as infrared light illumination.[99]

Composite systems of MnO_x with metals have been studied by different authors. For instance, MnO_x promoted with Pt for the degradation of toluene were tested. It was demonstrated that a 1 wt% Pt loading increased the catalytic oxidation of toluene by combining sunlight and heat.[97] For different applications, MnO_2 has been loaded with Ag, which induced the formation of oxygen vacancies and Mn^{3+}. The system presented antibacterial properties, induced by solar light irradiation. Ag induced the formation of vacancies as well as the local heating effect. In combination with MnO_2, the system promoted the formation of hot electrons and therefore the reactive (radical-type) species, which was enhanced by the thermo-photocatalytic effect.[100]

Composite catalysts formed by two oxides were synthesized by Yang *et al.*[101] MnO_x/TiO_2 was prepared for thermo-photocatalytic selective ethanol oxidation to acetaldehyde. The activity was tested and compared with TiO_2 (P25). The composites exhibited high catalytic activity compared to the reference. Moreover, the thermo-photocatalytic activity of the composites was compared with the photocatalytic counterpart. The authors determined that this type of composite provides a significant increase in the acetaldehyde production rate under UV-vis-IR irradiation. The enhancement of this catalytic activity in the selective oxidation of ethanol does not follow the traditional mechanism of photocatalysis, rather it follows a light-driven thermocatalysis mechanism. MnO_x/TiO_2 was also prepared by Ma *et al.* for the gas-phase degradation of the benzene pollutant under full-spectrum solar and visible-infrared illumination.[102] The results showed that the composites could efficiently transform solar energy into thermal energy, raising the surface temperature of the catalyst, resulting in improved catalytic activity. Amorphous manganese oxide supported on an anatase TiO_2 nanosheet was synthesized by Lan *et al.* for efficient UV-vis-infrared light-driven catalytic abatement of benzene.[103] The optimum composite (Mn/Ti molar ratio of 0.40) exhibited highly efficient thermo-photocatalytic activity and excellent durability. Ren *et al.* synthesized Pt–TiO_2/Ce–MnO_x compounds that showed excellent activity in the thermo-photocatalytic oxidation of benzene.[104] Wang *et al.* published two articles where similar composites formed with manganese oxide exhibited high thermo-photocatalytic activity.[105,106]

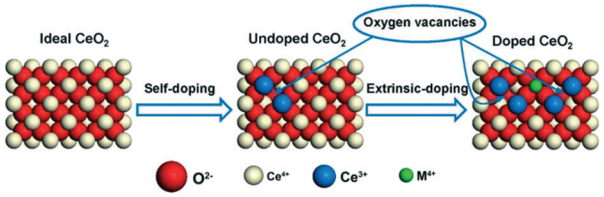

Fig. 15 Model of CeO_2 stoichiometric oxide projected along the ⟨1 0 0⟩ direction of the fluorite-type structure (left). This structure can transform into a non-stoichiometric oxide $CeO_{2-x/2}$ with the formation of Ce^{3+} and oxygen vacancies (middle). $Ce_{1-m}M_mO_{2-x/2-y}$ solid solutions can be formed by doping with smaller cations (M^{4+}) into CeO_2, generating Ce^{3+} together with oxygen vacancies (right). Reprinted with permission from ref. 112 (copyright® Elsevier 2018).

CeO_x-Based systems

Ceria (CeO_2) has been extensively studied in many areas, most notably, catalysis. However, in recent decades, it has been applied in thermo-photocatalytic reactions.[108–110] Ceria has significant use in the field due to its characteristic and high oxygen storage capacity (OSC), which is in turn related to the easy handing of cerium oxidation states ($Ce^{3+} \leftrightarrow Ce^{4+}$) and concomitant formation-annihilation of the oxygen vacancies.[111] CeO_2 displays a fluorite-type structure, where cerium cations have a coordination number of 8 and are centered in the cubes forming by eight nearest neighboring oxygen anions, while each oxygen anion is coordinated to four nearest neighboring cerium cations in a tetrahedral shape.[112] However, the ionic radius of Ce^{4+} may not be large enough to stabilize the fluorite structure; thus, some Ce^{4+} ions can be transformed into Ce^{3+} with the concomitant formation of oxygen vacancies. From the catalytic point of view, it is desirable to promote the redox conversion between Ce^{3+} and Ce^{4+}, which facilitates the formation of abundant anion (oxygen) defects and the concomitant release of new oxygen atoms. Fig. 15 shows the different structure of the ideal oxidized/reduced CeO_2 in the absence/presence of doping ions.

Verma *et al.* published an article where cerium oxide was synthesized with two different oxidation states in a core–shell type structure (CeO_2/Ce_2O_3).[108] The photocatalytic activity was evaluated using methyl orange (MO) under UV-vis irradiation and different temperatures. The authors reported that the self-degradation of MO under UV and visible illumination was negligible at all the temperatures tested. In contrast, the rate of CeO_2 (M) (calcined sample in vacuum) was 2.2 and 3.3 times higher than that of CeO_2 (S) (calcined sample in air) under UV and visible light, respectively. Both the samples were tested in the temperature range from 8 to 65 °C. When the temperature increased from 8 to 65 °C, the catalytic degradation increases by about 1.5 and 2.7 times under UV and visible light, respectively. In the case of CeO_2 (M), this behavior originates from the presence of an interface and

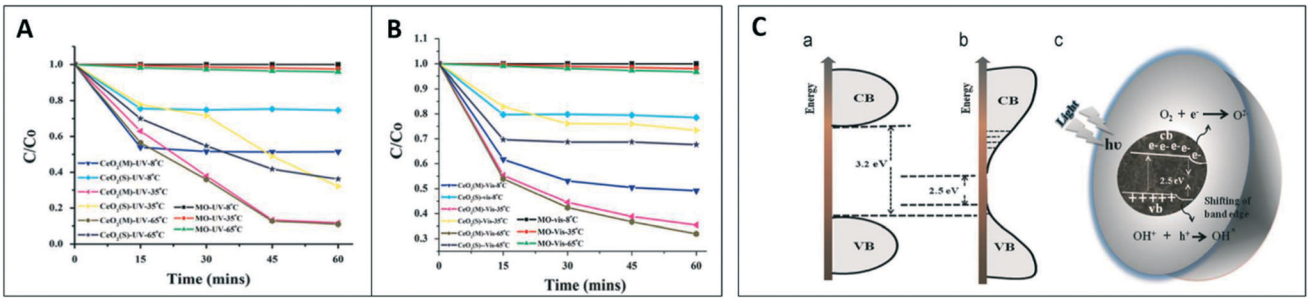

Fig. 16 UV- (A) and visible (B) light-photocatalytic degradation of methyl orange (MO) on CeO_2 (S) and CeO_2 (M) samples at the temperature range (8–65 °C). C) Schematic illustration of the density of states (DOS) before (a) and after vacuum annealing (b), and band diagram of CeO_2 (c). Reprinted with permission from ref. 108 (copyright® Elsevier 2015).

associated oxygen vacancies, positively affecting the separation and mobility of the charge carries, respectively. The largest increase under vis irradiation was ascribed to the extended absorption in the mentioned electromagnetic region. The temperature-dependent enhancement was mainly attributed to the enhancement of the carrier conductivity. The photo-excited electrons can migrate to the catalyst surface or recombine through thermalization. The heat dissipated in the process promotes the mobility of the carriers, facilitating their presence at the surface and subsequent involvement in the chemical reaction. This fact favors the development of a thermo-photocatalytic system, which has a higher reactivity than the photocatalytic system. Fig. 16 illustrated the density of states (DOS) before and after vacuum annealing. The last treatment favors the formation of the defects; therefore, both the valence and conduction bands increase in width, resulting in a decrease of the band gap (Fig. 16C b). The presence of CeO_2 and Ce_2O_3 favors the presence of defects to form mainly at the interface. The generated electrons after light absorption are trapped at the CeO_2 (core) and CeO_3 (shell) interface, which results in a decrease in the electron and hole recombination. Finally, the electrons are captured by oxygen on the surface forming the O^{2-} radicals, while the holes are captured by water or OH^- radicals, forming $OH^{\bullet}$, which degrades the MO.

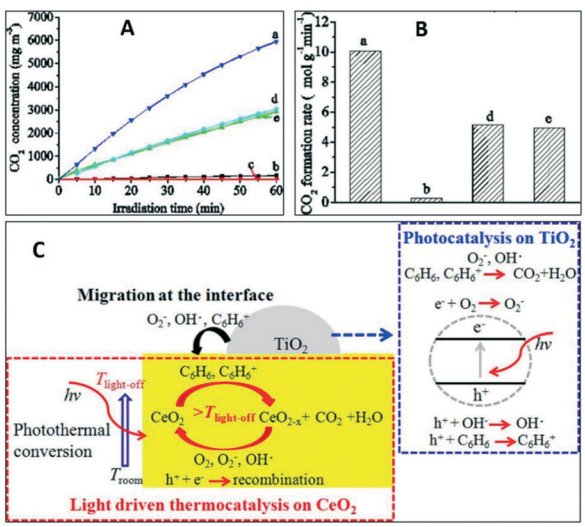

Fig. 17 CO_2 production (A) and r_{CO_2} (B) for benzene oxidation using: TiO_2/CeO_2-B (Xe lamp irradiation; thermo-photocatalysis) (a), TiO_2/CeO_2-B (b), and CeO_2 (c) (Xe lamp irradiation, *ca.* RT; photo-catalytic), TiO_2/CeO_2-B (irradiation >420 nm with higher light intensity (d), a mixture of TiO_2 and CeO_2 with the same Ti/Ce molar ratio as TiO_2/CeO_2-B under Xe lamp irradiation (e). C) Scheme presenting solar light-driven thermocatalysis and the synergetic effect between the photocatalysis on TiO_2 and thermocatalysis on CeO_2 taking place in a TiO_2/CeO_2 nanocomposite. Reprinted with permission from ref. 109 (copyright® Elsevier 2015).

The thermo-photo activity of CeO_2 has been studied together other oxides.[109,113,114] TiO_2/CeO_2 was synthesized by Zeng *et al.* and utilized for the gas-phase oxidation of benzene.[109] Three different samples with 0.021, 0.068, and 0.174 Ti/Ce molar ratios were synthesized. The samples were denoted as TiO_2/CeO_2-A, TiO_2/CeO_2-B, and TiO_2/CeO_2-C, respectively. The photocatalytic activity was tested and compared with CeO_2, TiO_2 (P25), and TiO_2, and the results show that the composites exhibited higher catalytic activity. The photocatalytic activity of CeO_2 and TiO_2/CeO_2-B was determined under Xe lamp irradiation near room temperature to confirm that the composites followed the conventional photocatalytic mechanism (Fig. 17A). On the other hand, the results revealed that at ~40 °C, the composites showed catalytic activity, while CeO_2 showed no activity. For the TiO_2/CeO_2-B composite, the CO_2 formation rate under the thermo-photo conditions (Fig. 17B(a)) was 36.4 times higher than the photocatalytic conditions (Fig. 17B(b)). The mechanism of the reaction is shown schematically in Fig. 17C. Light irradiation causes a considerable increase in the composite(s) temperature due to the infrared-triggered heating effect. When the temperature rises above the thermocatalytic light-off temperature ($T_{light\text{-}off}$), the thermocatalytic degradation of benzene occurs. The synergic effect was intimately connected with the promotion of the reduced Ce states, which is located at the interface of the TiO_2/CeO_2 composites (Fig. 17C).

Bellardita *et al.* published an article where TiO_2/CeO_2 was synthesized for the thermo-photo oxidation of 2-propanol, ethanol, and toluene.[113] For toluene elimination, thermo-photo degradation was studied from a kinetic perspective using the TiO_2/CeO_2 composite systems.[115] Complete analysis

using an intrinsic scheme with the rigorous analysis of both light and chemical variables was able to demonstrate changes in the energy of activation of the initial step of the toluene degradation, with lower values for thermo-photocatalysis with respect to thermal and photo alone values. This occurs parallelly to changes in the adsorption of the reactants under combined excitation. Therefore, a rigorous proof of a true synergistic effect between light and thermal energies was provided in this case. This kinetic effect takes place with the inclusion of radical species in a thermal-based reaction mechanism, a characteristic feature of a synergistic thermo-photo mechanism.[115]

Solar and thermo-catalysis led to a considerable decrease in the conversion temperature of organic compounds using composites containing Ce-based mixed oxide materials. $CeMn_xO_y/TiO_2$ has been studied by Liu *et al.* for benzene oxidation.[114] The results showed that the $CeMn_xO_y/TiO_2$ composites displayed much higher thermocatalytic activity than the composites such as CeO_2/TiO_2 and MnO_x/TiO_2. This fact has been related to the increased oxygen activity. In addition, the catalyst showed strong absorption in the entire solar spectral region, and was able to transform the absorbed solar energy into thermal energy, which leads to an increase in the temperature. This process results in light-facilitated thermocatalytic activity, with the promotion of the oxidation of benzene under full-spectrum solar, visible-infrared, and infrared illumination conditions. The same authors synthesized the $CeMn_xO_y$/(cryptomelane-type octahedral molecular sieve) OMS-2 composite, which showed a very efficient thermo-photocatalytic activity and a high stability under UV-vis-infrared illumination.[116] Hou *et al.* published two articles, where nanostructured Ce ion substituted OMS-2 was synthesized.[117,118] On the one hand, this type of compound was used for VOC purification. The results showed the efficient transformation of the absorbed solar energy to thermal energy with the help of the Ce ion-substituted OMS-2 catalyst.[117] The authors demonstrated that in this type of catalyst, the combination of photo-thermal conversion and thermocatalytic activity drives the catalysis with extremely high efficiency under full-spectrum solar, UV, vis, and IR illumination. On the other hand, the authors reported that Ce ion-substituted OMS-2 having Mn vacancies strongly promotes the catalytic activity.[118]

Finally, we briefly mention that different articles considered the use of CeO_2 together with metals as the co-catalysts.[119–121] Mao *et al.* synthesized a composite system formed by Pt nanoparticles partially embedded in the mesoporous CeO_2 nanorods, which exhibited very efficient catalytic activity and high stability for the solar light-driven CO_2 reduction.[122] The same authors studied the identical type of compound for the catalytic oxidation of benzene under UV-vis-IR light. The catalysts exhibited high catalytic activity due to sunlight-driven thermocatalysis caused by the combination of high thermocatalytic activity and a local heating effect originated from the surface plasmonic-type absorption taking place at the Pt component.[120] Pt was also used to promote the activity of the TiO_2/CeO_2 composite systems for hydrogen production from sacrificial bio-alcohols. An *operando* study analyzes the solid using X-ray absorption and the reactant-solid interface using infrared spectroscopy. From this, the authors elucidated the physicochemical basis of the synergistic thermo-photo effect displayed by the catalysts. The study showed that light affects a thermal mechanism, with the incidence of the specific oxidation-type steps of the sacrificial molecule and subsequent decarbonylation of the resulting intermediates, generating hydrogen concomitantly. The global effect is a unique mechanism with multiple effects in the surface chemical species. Overall, the simultaneous light-heat excitation triggers an increasing reaction rate by *ca.* 2 times (and a decreased overall energy consumption of *ca.* 30%) with respect to the additive combination of the thermal and photoreaction rates[123] Finally, Zhang *et al.* published an article where Ni/CeO_2 was synthesized for CO_2 reduction. The results showed that the catalyst exhibited high catalytic activity under UV-vis-IR due to efficient light-driven thermocatalytic activity.[119]

BiO_x-Based systems

Bi-Based composites have attracted much interest because of their high photocatalytic activity in visible light and relatively narrow band gap due to the hybridization of the O 2p and Bi $6s^2$ valence bands.[124] Li *et al.* synthesized a vacancy-rich BiO_{2-x} monolayer able to absorb light throughout the full solar spectrum.[125] This catalyst showed enhanced photon absorption and response due to the formation of electronic states near the conduction band minimum. The increased catalytic performance of this material compared to BiO_2 bulk was attributed to the (Bi–O associated) vacancy V'''_{Bi-O} as demonstrated using positron annihilation spectroscopy. Moreover, the presence of V'''_{Bi-O} defects in the BiO_{2-x} monolayer promoted the separation of the charge carrier species, avoiding charge recombination. All these phenomena resulted in the enhancement of the catalytic activity. Liu *et al.* synthesized a nanoradiosensitizer tool using ultrathin BiO_{2-x} nanosheets (NSs) modified with Tween 20 (T-BiO_{2-x} NSs). It facilitates overcoming hypoxia-induced radioresistance as well as to increase the radiation therapy efficiency.[126] High-Z elements such as bismuth have been explored as radiosensitizers to increase the radiosensitivity of tumors because these materials are capable of absorbing and depositing a significant amount of radiation in the tumor area.[127,128] BiO_{2-x} nanosheets have exhibited high photocatalytic performance due to the presence of defects in their structure. The presence of defects increases the charge carrier separation, reduces the band gap, and increases the valence band edge energy. In addition, the presence of oxygen vacancies also promotes the catalytic activity of the BiO_{2-x} nanosheet.

Li *et al.* published an article where Ni^{2+}-doped BiO_{2-x} nanosheets were synthesized.[129] The structural properties of

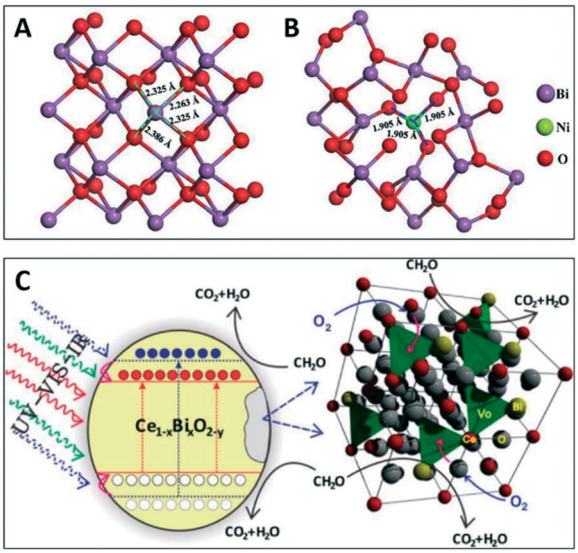

Fig. 18 DFT calculations. Crystal structures of (A) bare BiO_{2-x} and (B) Ni^{2+}-doped BiO_{2-x}. Proposed mechanism of Bi-induced synergistic thermo-photocatalysis (C). A and B) Reprinted with permission from ref. 129 (copyright® Elsevier 2020). C) Reprinted with permission from ref. 134 (copyright® ACS 2013).

BiO_{2-x} and Ni^{2+}-doped BiO_{2-x} were analyzed to determine the effect of Ni. The XRD patterns indicated that BiO_{2-x} displays the cubic phase of BiO_{2-x} (JCPDS No. 47-1057). The Ni^{2+}-doped BiO_{2-x} patterns were also obtained for samples with different amounts of Ni (2%, 4%, 6%, and 8%) and the results showed that all of them can also be indexed in the cubic phase of BiO_{2-x}. No other peaks other than that for BiO_{2-x} were observed, which was interpreted as a result of the Ni^{2+} incorporation into the lattice. It was also observed that the (111) and (200) peaks of the doped sample were shifted towards higher 2θ.[130] The detection of a shift in the diffraction peaks reflects the decrease in the Ni–BiO_{2-x} interplanar spacing (Bragg's law),[131] resulting from the substitution of Bi ions with larger ionic radius by the smaller Ni^{2+}. Fig. 18A and B includes data from the DFT calculations. In the Ni-containing structure, the Ni–O first shell coordination distance is shortened, with the concomitant formation of a distorted local structure of Ni^{2+}-doped BiO_{2-x}. In addition, the total density of states (TDOS) and partial density of states (PDOS) showed that the introduction of Ni^{2+} into the structure triggered the formation of a new energy level.

This electronic level allows electrons to be excited, providing additional charge carrier species and favoring the catalytic activity.

Oxygen vacancy-rich Bi_2O_4–Bi_4O_7–BiO_{2-x} composites were synthesized by Jia *et al.* for UV-vis-NIR activated high efficient photocatalytic degradation of bisphenol A.[132] The authors demonstrated that Bi_2O_4–Bi_4O_7–BiO_{2-x} nanocomposites rich in oxygen vacancies exhibit much higher catalytic efficiency than other single or binary bismuth oxide systems under UV, vis, and NIR light illumination conditions. These results together with DFT calculations suggested that type-II charge transfer and Z-scheme with oxygen vacancies as electron–hole mediators can occur at the interfaces. Hence, efficient charge separation and high full-spectrum sunlight utilization can take place. One-dimensional/two-dimensional core–shell-structured Bi_2O_4/BiO_{2-x} heterojunctions were studied by Li *et al.* for highly efficient full-spectrum photocatalysis.[133] The results showed that the composite exhibited broad absorption from 200 to *ca.* 2500 nm. Moreover, the Fermi level position suggested that the material would have higher carrier mobility compared to Bi_2O_4 and BiO_{2-x}, which facilitates the separation of the charge carrier species. In short, the high photocatalytic activity of the Bi_2O_4/BiO_{2-x} composite could be attributed to the high adsorption, high mobility of charge carriers, and fast charge transfer across the heterointerface.

Jiang *et al.* published an article using a Bi-doped ceria thermo-photocatalyst (fluorite-doped $Ce_{1-x}Bi_xO_{2-\delta}$ nanorods).[134] CeO_2 (C) and $Ce_{1-x}Bi_xO_{2-\delta}$ were tested under light irradiation at 25 °C and 80 °C with/without light to simulate photocatalysis, thermocatalysis, and thermo-photocatalysis. The results showed that the binary Ce–B catalyst was much more efficient than the bare ceria catalyst under all the conditions. According to the authors, the introduction of Bi atoms and concomitant anionic vacancies are at the origin of the synergistic coupling of low-temperature catalysis in a photocatalytic-dominated mechanism. In addition, the presence of ceria and Bi shows mixed ionic and electronic conductivity, and therefore, enhanced charge carried mobility. The doped catalysts can be considered as a combination of an n-type semiconductor and an oxygen ion conductor. Fig. 18C illustrates the proposed mechanism. The presence of Bi^{3+} in the structure enhances the absorption of visible light, and improves the redox capability of the oxide at low temperatures. Besides this, the vacancies significantly promote the migration of oxygen ions to the surface positions, opening the possibility of obtaining activity at low temperature. Finally, the recombination of charge carriers is effectively diminished due to the trapping effects related to the defects, with the ionic and electronic conductivity boosted (with respect to photocatalysis) by the temperature increase originated from the absorption of IR light. All these effects make it possible to benefit from the IR region of the solar spectrum and thus increase the catalytic performance.

InO_x-Based systems

Indium oxide is another system with significant use in the context of the thermo-photo research field. In this case, the defect structure exploited is mostly related to the generation of a mixed oxide/hydroxyde structure in the nanostructured materials. From the oxide, the generation of oxygen vacancies is achieved with presence of hydroxyl entities as the charge neutral species. Such a type of system has been initially used for CO_2 reduction to several products such as CO, CH_4, and

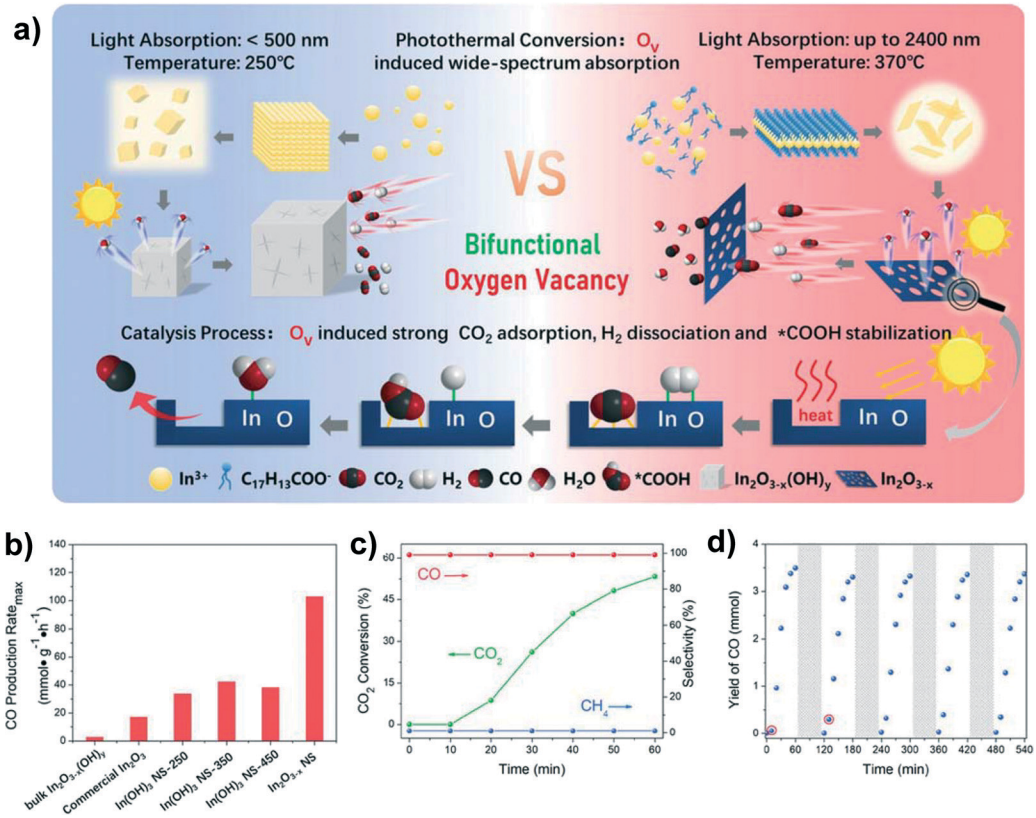

Fig. 19 Scheme of the thermo-photocatalytic reaction system and indium oxide-based catalyst (a and b). Catalytic rates *vs.* temperature in light (245.7 mW cm^{-2}) and dark conditions (c). CO production rates *vs.* light intensity at 458 K (d). Reprinted with permission from ref. 138 (copyright® Wiley 2019).

CH_3OH. Thus, indium oxide, initially explored in the form of nanorods and nanoparticles, is able to catalyze chemical reactions such as the reverse water gas shift (generating CO) or methanol synthesis using carbon dioxide as the raw material. Joint spectroscopic and DFT studies showed that the activity of the indium-containing powders is closely connected with the broadband absorption of the solid and the photo to thermal conversion of low energy photons but also with the surface properties of the solids. Concretely, with specific Lewis acidic and basic active frustrated Lewis pairs (FLPs) sites ($O^{\delta-}$–$In^{\delta+}$) generated (or promoted) under light and able to significantly decrease the activation energy of the initial carbon dioxide reduction step.[135] Progressing in the heterogenization of the material, some works studied the activity of black indium oxide, outperforming previous ("non-black") materials in the form of nanorods/nanoparticles and selectively generating CO from CO_2. Similar to titania, black powder is presumed to be formed by a core, less defective indium oxide, and a strong defective outer layer.[136] The same black material in the form of nanosheets allowed an even more fruitful combination of light and heat. As shown in Fig. 19, a huge increase in the light absorption, covering almost the full solar spectrum, facilitates the rise of the temperature if compared with other more conventional and already mentioned morphologies. Moreover, the defect-rich nanosheet appears to stabilize formate-type COOH* species with respect to carbonates and hydrogen-carbonates species, significantly decreasing the activation energy of the reaction and boosting the activity. The nanosheet morphology also shows stability under cycling experiments.[137]

Thermo-photocomposite systems using indium oxide have been mostly explored in the presence of components acting as heaters and will be considered in the next section of this work.

4. Heating materials

The last type of thermo-photoactive systems consider the use of materials specifically devoted to the catalytic utilization of the thermal energy. This could be carried out with the help of external or internal heating sources, as depicted in Fig. 2C. External heating may find applications in the current context for specific composite materials where actives sites are somehow localized at specific positions, such as interfaces between components having one thermal and the other photonic-oriented capabilities.[7] In any case, as mentioned in section 1 of this review, the more general use of external heating could consider systems that have both thermal and optical properties, leading to active catalytic functionality. For our purposes, most works use external heating consider plasmonic and/or defective oxides with inherent thermo-photocatalytic activity having complex physicochemical roots.

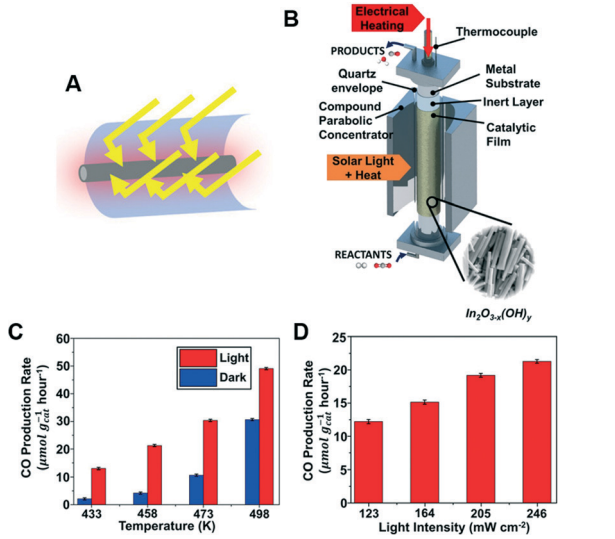

Fig. 20 A) Schematic illustration of the formation mechanism and catalytic process of bulk In_2O_3 and 2D black In_2O_{3-x} nanosheets. B) Rates of CO production for bulk $In_2O_{3-x}(OH)_y$, commercial In_2O_3, $In(OH)_3$ nanosheets (treated at different annealing temperatures) and 2D black In_2O_{3-x} nanosheets. C) Thermo-photo CO_2 conversion and selectivity for $In(OH)_3$ nanosheets. D) Stability cyclic test. Reprinted with permission from ref. 137 (copyright® Wiley 2019).

The examples of such composite catalysts have been presented in previous sections of this review article using, for example, copper, tungsten, or cerium oxides. Another possibly is the so-called internal heating. As a first class of "internal heating" materials, we can highlight the case of non-catalytic materials with high efficiency in absorbing low energy photons *via* phonons (Fig. 2C).[7,9] Metals used as foils (therefore, with low surface area and catalytic activity) such as Cu or Al (normally surface passivated or modified to allow easy interface contact with catalysts) or non-catalytic semiconducting or insulating materials such as Si, WN, and others, are frequently utilized. As depicted in Fig. 2C, the optical properties of the materials are critical to ensure the adequate handling of the different light wavelengths through a significant number of phenomena including adsorption, scattering, and and/or reflectance. To this, we should add the heat-conductive and/or radiative properties of the "heater" component. Such materials, in form of films, wires, *etc.*, have been utilized in combination with, for example, indium oxide-hydroxide active catalytic materials. An interesting example utilizes the indium oxy-hydroxide and an Al film to benefit from both external and internal heating effects using a typical photocatalytic parabolic-type collector reactor for sunlight illumination.[138] Fig. 20 depicts the reactor (panels A and B) and the activity of the catalyst for CO_2 reduction (to render almost exclusively CO) under light and dark conditions at different temperatures (panel C) and under different illumination intensity values (panel D). Both light intensity and temperature have a strong effect on the catalytic output, indicating the significance of light-induced effects in a presumably thermal-based reaction. The activity under thermo-photo conditions appears stable for long term operation and decreases by the energy input *ca.* 30%, utilized under thermal conditions. This clearly indicates the suitability of the system for future industrial application. Others catalytically-active oxide-based materials tested under similar thermo-photo conditions are amorphous yttrium oxide promoted with nickel[139] or ruthenium oxide.[140]

"Internal" heating systems can also make use of components with the preferential non-radiative de-excitation of relatively low energy photons, particularly low energy visible and (the whole range of) infrared photons. This requires "low band gap energy" materials and can generate localized thermal energy that can be exploited at the nanoscale. As said previously, non-radiative de-excitation always occur in all photoactive materials (presenting a complex dependence of morphological and structural properties) and is thus contributing, to some extent, to the activity of many systems described in the previous sections. In any case, here, we describe systems where this phenomenon may be significant, particularly for the fruitful use of low energy (typically infrared) photons. Such localized heating at the nanoscale level can be achieved using minor (by weight or composition) components within the composite systems. The minor components can be located strategically near the active centers of the composite systems and this would generate specific local heating effects. In specific cases, such components can also be active catalytic materials. Mostly chalcogenides (outside the scope of this review) are used in this context due to their limited band gap energy and, for most cases, dominant non-radiative de-excitation. However, within oxide systems, the presence of Ag_2O_x in the composite systems usually enables the profiting of low energy (near infrared) photons, as depicted in Fig. 21.

The Ag_2O_x-containing composite with a major bismuth oxyhalide component is a relatively explored system but its utility in thermo-photocatalysis has been only analyzed recently. The system is capable of using UV, visible, and near infrared (up to 940 nm) photons with efficient charge separation taking place for all excitation wavelengths and, therefore, high activity. Thermal effects play a significant role in promoting the catalytic activity for higher wavenumber excitation photons. Nevertheless, the combination of pure photonic and heating effects and the (quantitative) assessment of their respective contributions requires further work.[141] Other silver oxide-containing composite systems having titania as the main component were used in thermo-photocatalysis for hydrogen production[142] or dye degradation.[143]

Finally, we can mention the potential interest of the localized internal heating pathway generated through other physical phenomena currently not explored. Up-conversion has been mostly tested in the context of converting visible or near-infrared photons to UV (or high energy visible) photons. However, it is well known that the process has a low quantum yield, with most cases below having 2%.[9] This opens the possibility of using the dominant non-radiative de-

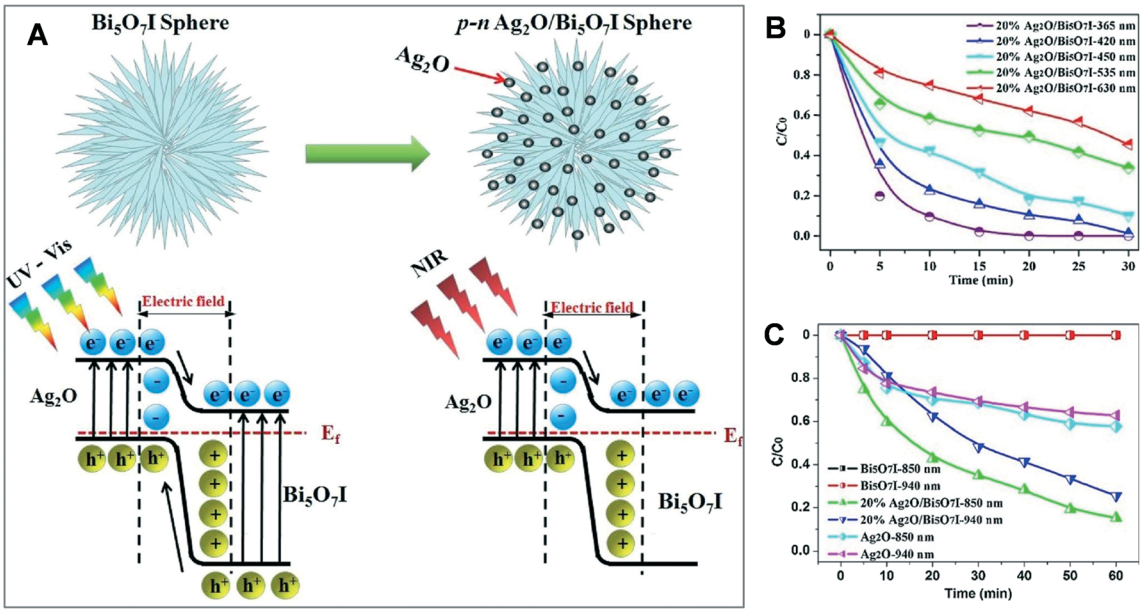

Fig. 21 A) Schematic representation of the morphological characteristics and charge carrier handling behavior of Ag_2O/Bi_5O_7I composites under different illumination sources. B) Photocatalytic activities of a 20% Ag_2O/Bi_5O_7I composite for bisphenol A degradation under UV (365 nm) and visible (420, 450, 535, and 630 nm) light irradiation. C) Photocatalytic activities of pure Bi_5O_7I, 20% Ag_2O/Bi_5O_7I composite, and Ag_2O samples in the bisphenol A degradation process under NIR light irradiation (850 and 940 nm). Reprinted with permission from ref. 141 (copyright® Elsevier 2018).

excitation as a source of rather localized heating, for example, locating up-converting species at the surface of the photoactive materials. To our knowledge, this type of technology has not been explored to date. Finally, we can recall (as described in section 1) that pyroelectric materials may also be useful in the thermo-photocatalytic context.[19] However, from a practical point of view, the use of these materials demands both expensive and poorly controllable composite catalyst architectures (requiring the presence of additional "active" phases such as titania and careful preparation to obtain the desired oxides with pyroelectric/piezoelectric properties) and complex/expensive reactor operation, thus limiting the usefulness for general application. Moreover, to date, they are normally tested in dye degradation reactions, with limited information concerning more interesting photocatalytic processes.

5. From the present to the future

The combination of thermal and light energy in catalytic processes presents an energy scenario with significant differences compared to the thermal or photo processes individually. The basic description presented in section 1 gives evidence of the fact that energy excitation and de-excitation processes occur with different physical rules in thermal and photonic reactions. Thus, the corresponding combination of energy sources explores a new and essentially unknown field. Nevertheless, rapid progress shows the utility of oxide-based materials in thermo-photocatalytic processes. In particular, herein, we analyzed composite systems with oxide-based components having important catalytic role(s). To this end, we organized oxides within three different groups. Composite materials are thus classified as those working under plasmonic effects, controlled by defect-derived phenomena or having a wise handling of heating effects coming for conductive/convective/radiative sources. Indeed, as composite systems are complex in nature, they can (and it is so, in fact) use more than one of these phenomena simultaneously. Moreover, as explained previously, most of the (above described) physicochemical properties of the solids sustaining thermo-photocatalytic activity are interrelated and their effect on the catalytic activity cannot be ignored. Thus, the described classification mostly takes into account the phenomenon that is considered to be the most important with current, available information rather than a real classification. Yet, we note that the physics behind (here defined) plasmonic, defect-derived, and thermal systems is clearly established for single component, well-defined materials and may thus serve as a firm ground for the analysis of the thermo-photo behavior of the composite systems.

Plasmonic-based oxide-containing composite systems have been analyzed using tungsten, molybdenum, and copper oxides as the representative examples of the research. Other oxides such as ruthenium oxide have been mentioned but are significantly less explored. The plasmonic chemistry is particularly devoted to the use of visible and near infrared photons and can be easily combined with UV-absorbers with important thermal and photo activity as that of titania. For defect-related systems, we presented examples of composite systems having cobalt, manganese, cerium, bismuth, and indium oxides. As occurring with plasmonic materials,

Table 1 Possible general types of thermo-photoreactions classified according to the mechanistic and kinetic criteria

Mechanism	Kinetic effects	Experimental observables
Photo-type	Thermal RDS[a]	Energy of activation
	Thermal effect in relevant (radical or poisoning species)	Surface coverage of species
		Adsorption energy
		Reaction order
Thermal-type	Photo RDS[a]	Energy of activation
	Photonic effect in relevant (active or poisoning) species	Surface coverage of species
		Adsorption energy
		Reaction order
Combined	New RDS (new relevant chemical species)[a]	All above-mentioned

[a] RDS: rate-determining step.

combination with UV absorbers allow to profit from the complete solar spectrum in the thermo-photo processes. Defect-type systems of relatively poor photocatalytic oxides are also commonly utilized to profit from heat using light-responsive oxides. Finally, we described composite materials similar to the benefit from (nano)heating components and containing indium and silver oxides as the examples, as well as some others described in previous sections such as copper, tungsten, or cerium oxides. This last family encompasses oxide materials with a role in the thermo-photocatalytic process defined by the use of external or internal heating processes and, in the latter case, by the way light to thermal energy conversion takes place through different de-excitation processes considering catalyst phonons or "direct" non-radiative de-excitation after light absorption. Among thermo-photoactive systems, the review also pointed out (up-to-date) less explored opportunities that benefit from the combination of light and heat. Particularly important could be the use of heavily doped oxides for broadband plasmonic components, up-conversion cation species used at surface modifiers to handle local heating issues, or the utilization of pyroelectric oxides able to handle the Seebeck effect.

For all the systems mentioned in this work, the complex nature of the thermo-photo process was evident. In spite of this, Table 1 introduces the main types of effects with mechanistic and kinetic relevance and thus with potential beneficial effects in catalysis under dual light-heat excitation.[5,6,7] The classification attempts to give a simple rationalization of the works reviewed outside the main physicochemical phenomena commanding activity, and it is used herein to render an alternative yet complementary classification of the oxide-based catalytic systems presenting thermo-photo activity. The results reviewed in this work indicate that active oxides such as titania can follow photo-type or -dominated reaction mechanisms while oxides with low photocatalytic activity, such as cobalt or manganese oxide, would follow thermal-type mechanisms. In addition, in specific cases, similar to those having ceria–titania or highly active interfaces, appearing in the composite systems (and generated by a strong interaction between the components), a unique type of mechanism can take place. This can be called combined or true thermo-photo mechanism. Of course, not all (composite) systems containing a single oxide would necessarily follow a single type of mechanism. As a simple example, the active interfaces between the oxide components can generate, as mentioned, unique systems, without direct relation (in terms of mechanism/kinetics) with the parent systems. An additional example would be the doping of a photo-type oxide with critical thermal effects. If the doping cation has inherent chemical activity and introduces relevant thermal effects, a change in the mechanism type may take place.

Under this framework and considering photo or thermo-type dominated mechanisms, when important thermo-photo effects are observed, the specific kinetic effects associated with the "secondary" energy source are expected. Most of the results suggest two different options (with common physical roots in these two photo or thermo-type dominated mechanisms). These two options concern (i) the alternation of the rate determining step, or (ii) of some properties of the relevant chemical species, either active (but not involved in the rate determining step) or poisoning intermediates of the reaction. We may think, for example, in the case of specific radical species under a thermal-type mechanism. A potential (significant) influence of the superoxide radicals may not alter the apparent energy of activation of a thermal-based reaction (Mars–van Krevelen, for example) but may alter the kinetics (though the inclusion of excited electrons able to generate the superoxide radical species in the early state of oxygen activation, in turn influencing the corresponding reactant consumption or product generation rate equations). The experimental observables included in the last column of the table ultimately end in changes in both the activity and selectivity from (both thermal and photo alone parent) the chemical process and may allow to distinguish the different types of mechanisms and main kinetic effects in each case of single-source-dominated mechanisms. On the contrary, when a novel thermo-photo (combined) mechanism takes place, all the above-mentioned experimental observables would be modified. Note that the inclusion of light in all the mechanisms of Table 1 requires to utilize rigorous intrinsic kinetics schemes with the use of the rate of the photon absorption as the main tool to include the light-related

effects.[144] Without using adequate analytical tools, the results from mechanistic/kinetic insights can be misleading.

The full interpretation of a thermo-photocatalytic process would thus require to rigorously analyze the mechanistic and kinetic aspects of the reaction as well as to determine the main light or heat-related (plasmonic, defect, thermal, combination, *etc.*) physicochemical phenomenon/phenomena sustaining activity. For the latter, advanced *operando* schemes using spectroscopies would be the key to providing accurate information. On the other hand, from an applied point of view, the progress in producing cheap catalytic formulations as well as to fit process technology (particularly reactor design and operation) to those currently used in thermal catalysis may drive the future of the thermo-photocatalytic field. In this quest, the mentioned thermo-photo oxide-based composite systems has shown activity in a significant number of reactions concerning pollutant elimination and valorization, selective oxidation, hydrogen production from biomolecules or water, and production of valuable chemicals from carbon dioxide. In short, thermo-photo materials can have the same versatility showed by conventional catalysis. On the other hand, the use of thermo-photocatalysts is sustained by frequent synergy between the energy sources, independent of the type of mechanism or physicochemical phenomena ruling the activity. The synergy can be related primary to the decrease in the energy consumption with respect to the additive sum of the thermal and photo alone processes. The assessment of this critical point requires the further development of the theoretical framework to describe thermo-photocatalysis as well as a rigorous energy balance of the process. In addition, the beneficial effects can be extended to other points, with emphasis on enhanced or modified (to valuable products) selectivity due to the unique energy playground of the thermo-photo reactions.

In summary, the progress in the field would require improvements in the development of composite systems with components designed to profit from plasmonic, defect-derived, and thermal-alone effects and having engineered contact among the components. In parallel, it would require developments leading to the full understanding of the catalytic behavior through the setting-up of firm structure–activity relationships established with the help of new *operando* spectroscopic tools, innovative (intrinsic-type) spectrokinetic schemes and analyses, as well theoretical tools relaying the use of time-dependent DFT schemes.[5,6,144–148] In addition, the development of specific thermo-photo reactors will significantly boost the technological potential of the field. In this case, interesting novel aspects can be related to further developing the current, well-defined thermo-based reactors to include a light source in the most efficient way, for example, using optical fibers, monolithic architectures with controlled optical properties, as well as the wise combination of light and heat energy sources from the sun using parabolic, Fresnel lens, or other collector-type reactor components.[6,138,147,149] In short, new research can show that the thermo-photo combination can have an impact on the future development of catalysis and could pave the way for creating new, advanced (thermo-photo)catalytic processes. Simultaneously, it can open the door for the efficient use of solar light, the most widely available and renewable energy source, in conventional thermo-catalytic reactions.

Author contributions

IB-N conceptualization, methodology, writing – review & editing; NG-C conceptualization, methodology, writing – review & editing; AK conceptualization, methodology, visualization, writing – review & editing, supervision, funding acquisition, project administration; MFG conceptualization, methodology, writing – review & editing, supervision, funding acquisition, project administration.

Conflicts of interest

There are no conflicts to declare.

Acknowledgements

Authors are thankful to "Ministerio de Ciencia e Innovación" (Spain) for supporting the work carried out through the PID2019-105490RB-C31 grant. I. B.-N. and N. G.-C. would like to thank MICIN for, respectively, doctoral FPI (BES-2017-080069) and post-doctoral JyD (FJC2019-039969) fellowships. M. F. G. is fully indebted to Prof. F. Fernández-Martín for general discussions.

References

1 J. C. Vedrine, in *Fundamentals of heterogeneous catalysis*, 2018, pp. 1–41.
2 B. Ohtani, *Phys. Chem. Chem. Phys.*, 2014, **16**, 1788–1797.
3 A. Kubacka, M. Fernández-García and G. Colón, *Chem. Rev.*, 2012, **112**, 1555–1614.
4 B. Liu, X. Zhao, C. Terashima, A. Fujishima and K. Nakata, *Phys. Chem. Chem. Phys.*, 2014, **16**, 8751.
5 R. Ma, J. Sun, D. H. Li and J. J. Wei, *Int. J. Hydrogen Energy*, 2020, **45**, 30288–30324.
6 N. Keller, J. Ivanez, J. Highfield and A. M. Ruppert, *Appl. Catal., B*, 2021, 120320.
7 V. Nair, M. J. Muñoz-Batista, M. Fernández-García, R. Luque and J. C. Colmenares, *ChemSusChem*, 2019, **12**, 2098–2116.
8 P. Verma, K. Mori, Y. Kuwahara, R. Raja and H. Yamashita, *Mater. Adv.*, 2021, **2**, 880–906.
9 L. Wang, X. Xu, Q. Cheng, S. X. Dou and Y. Du, *Small*, 2021, **17**, 1904107.
10 Z. Wang, H. Song, H. Liu and J. Ye, *Angew. Chem., Int. Ed.*, 2020, **59**, 8016–8035.
11 K. Czelej, J. C. Colmenares, K. Jabłczyńska, K. Ćwieka, Ł. Werner and L. Gradoń, *Catal. Today*, DOI: 10.1016/j.cattod.2021.02.004, in press.
12 A. Kubacka, U. Caudillo-Flores, I. Barba-Nieto and M. Fernández-García, *Appl. Catal., A*, 2021, **610**, 117966.

13 S. Ishii, S. L. Shinde and T. Nagao, *Adv. Opt. Mater.*, 2019, **7**, 1800603.
14 N. Wu, *Nanoscale*, 2018, **10**, 2679–2696.
15 A. O. Govorov, H. Zhang and Y. K. Gun'ko, *J. Phys. Chem. C*, 2013, **117**, 16616–16631.
16 C. S. Kumarasinghe, M. Premaratne, S. D. Gunapala and G. P. Agrawal, *Phys. Chem. Chem. Phys.*, 2016, **18**, 18227–18236.
17 A. Agrawal, S. H. Cho, O. Zandi, S. Ghosh, R. W. Johns and D. J. Milliron, *Chem. Rev.*, 2018, **118**, 3121–3207.
18 T. S. Rajaraman, S. P. Parikh and V. G. Gandhi, *Chem. Eng. J.*, 2020, **389**, 123918.
19 C. Wang, N. Tian, T. Ma, Y. Zhang and H. Huang, *Nano Energy*, 2020, **78**, 105371.
20 J. Chen, W. Luo, S. Yu, X. Yang, Z. Wu, H. Zhang, J. Gao, Y.-W. Mai, Y. Li and Y. Jia, *Ceram. Int.*, 2020, **46**, 9786–9793.
21 M. Wang, B. Wang, F. Huang and Z. Lin, *Angew. Chem., Int. Ed.*, 2019, **58**, 7526–7536.
22 S. Tu, H. Huang, T. Zhang and Y. Zhang, *Appl. Catal., B*, 2017, **219**, 550–562.
23 H. A. Atwater and A. Polman, *Nat. Mater.*, 2010, **9**, 205–213.
24 V. Garg, B. S. Sengar, V. Awasthi, Aaryashree, P. Sharma, C. Mukherjee, S. Kumar and S. Mukherjee, *RSC Adv.*, 2016, **6**, 26216–26226.
25 G. C. Phan-Quang, X. Han, C. S. L. Koh, H. Y. F. Sim, C. L. Lay, S. X. Leong, Y. H. Lee, N. Pazos-Perez, R. A. Alvarez-Puebla and X. Y. Ling, *Acc. Chem. Res.*, 2019, **52**, 1844–1854.
26 W. Li, X. Zhao, Z. Yi, A. M. Glushenkov and L. Kong, *Anal. Chim. Acta*, 2017, **984**, 19–41.
27 J. Chen, J. Feng, F. Yang, R. Aleisa, Q. Zhang and Y. Yin, *Angew. Chem.*, 2019, **131**, 9376–9382.
28 Q. Shi, H. Xia, P. Li, Y.-S. Wang, L. Wang, S.-X. Li, G. Wang, C. Lv, L.-G. Niu and H.-B. Sun, *Adv. Opt. Mater.*, 2017, **5**, 1700442.
29 S. K. Cushing, J. Li, F. Meng, T. R. Senty, S. Suri, M. Zhi, M. Li, A. D. Bristow and N. Wu, *J. Am. Chem. Soc.*, 2012, **134**, 15033–15041.
30 X. Zhu, C. Jin, X.-S. Li, J.-L. Liu, Z.-G. Sun, C. Shi, X. Li and A.-M. Zhu, *ACS Catal.*, 2017, **7**, 6514–6524.
31 U. Caudillo-Flores, I. Barba-Nieto, M. N. Gómez-Cerezo, A. Martínez-Arias, M. Fernández-García and A. Kubacka, *ACS Sustainable Chem. Eng.*, 2019, **7**, 15671–15683.
32 B. Xie, E. Lovell, T. H. Tan, S. Jantarang, M. Yu, J. Scott and R. Amal, *J. Energy Chem.*, 2021, **59**, 108–125.
33 L. Liang, X. Li, Y. Sun, Y. Tan, X. Jiao, H. Ju, Z. Qi, J. Zhu and Y. Xie, *Joule*, 2018, **2**, 1004–1016.
34 P. Verma, K. Yuan, Y. Kuwahara, K. Mori and H. Yamashita, *Appl. Catal., B*, 2018, **223**, 10–15.
35 Y. Z. Chen, Z. U. Wang, H. Wang, J. Lu, S. H. Yu and H. L. Jiang, *J. Am. Chem. Soc.*, 2017, **139**, 2035–2044.
36 U. Caudillo-Flores, G. Agostini, C. Marini, A. Kubacka and M. Fernández-García, *Appl. Catal., B*, 2019, **256**, 117790.
37 X. Li, Y. Yan, Y. Jiang, X. Wu, S. Li, J. Huang, J. Li, Y. Lin, D. Yang and H. Zhang, *Nanoscale Adv.*, 2019, **1**, 3941–3947.
38 H. Cheng, T. Kamegawa, K. Mori and H. Yamashita, *Angew. Chem., Int. Ed.*, 2014, **53**, 2910–2914.
39 C. Han, Q. Quan, H. M. Chen, Y. Sun and Y. J. Xu, *Small*, 2017, **13**, 1–11.
40 Y. Zhao, Z. C. Feng, Y. Liang and H. W. Sheng, *Appl. Phys. Lett.*, 1997, **71**, 2227–2229.
41 D. Mateo, J. L. Cerrillo, S. Durini and J. Gascon, *Chem. Soc. Rev.*, 2021, **50**, 2173–2210.
42 L. Wang, Y. Wang, Y. Cheng, Z. Liu, Q. Guo, M. N. Ha and Z. Zhao, *J. Mater. Chem. A*, 2016, **4**, 5314–5322.
43 Y. Li, C. Wang, H. Zheng, F. Wan, F. Yu, X. Zhang and Y. Liu, *Appl. Surf. Sci.*, 2017, **391**, 654–661.
44 Z. Lou, Q. Gu, L. Xu, Y. Liao and C. Xue, *Chem. - Asian J.*, 2015, **10**, 1291–1294.
45 J. Li, G. Chen, J. Yan, B. Huang, H. Cheng, Z. Lou and B. Li, *Appl. Catal., B*, 2020, **264**, 118517.
46 C. Feng, L. Tang, Y. Deng, J. Wang, W. Tang, Y. Liu, Z. Chen, J. Yu, J. Wang and Q. Liang, *Chem. Eng. J.*, 2020, **389**, 124474.
47 M. J. Landry, A. Gellé, B. Y. Meng, C. J. Barrett and A. Moores, *ACS Catal.*, 2017, **7**, 6128–6133.
48 Z. Lou, Q. Gu, Y. Liao, S. Yu and C. Xue, *Appl. Catal., B*, 2016, **184**, 258–263.
49 Y. Ren, C. Li, Q. Xu, J. Yan, Y. Li, P. Yuan, H. Xia, C. Niu, X. Yang and Y. Jia, *Appl. Catal., B*, 2019, **245**, 648–655.
50 M. H. Vu, C. C. Nguyen and T. O. Do, *ACS Sustainable Chem. Eng.*, 2020, **8**, 12321–12330.
51 S. Sun, X. Chang, L. Dong, Y. Zhang, Z. Li and Y. Qiu, *J. Solid State Chem.*, 2011, **184**, 2190–2195.
52 M. Yan, G. Li, C. Guo, W. Guo, D. Ding, S. Zhang and S. Liu, *Nanoscale*, 2016, **8**, 17828–17835.
53 X. Y. Sun, F. J. Zhang and C. Kong, *Colloids Surf., A*, 2020, **594**, 124653.
54 Y. Huang, H. Xu, D. Luo, Y. Zhao, Y. Fang, Q. Guo, Y. Wei, L. Fan and J. Wu, *J. Alloys Compd.*, 2019, **806**, 418–427.
55 Z. Zhang, J. Huang, Y. Fang, M. Zhang, K. Liu and B. Dong, *Adv. Mater.*, 2017, **29**, 1606688.
56 J. Yan, C. Wang, H. Ma, Y. Li, Y. Liu, N. Suzuki, C. Terashima, A. Fujishima and X. Zhang, *Appl. Catal., B*, 2020, **268**, 118401.
57 H. Yin, Y. Kuwahara, K. Mori, H. Cheng, M. Wen, Y. Huo and H. Yamashita, *J. Phys. Chem. C*, 2017, **121**, 23531–23540.
58 G. Collins, A. Lonergan, D. McNulty, C. Glynn, D. Buckley, C. Hu and C. O'Dwyer, *Adv. Mater. Interfaces*, 2020, **7**, 1901805.
59 X. Xu, G. Fang, J. Shang, K. Liu, Y. Bao, Y. Yang, Y. Liu and B. Dong, *J. Mater. Sci.*, 2020, **55**, 2958–2966.
60 A. Kubacka, M. J. Muñoz-Batista, M. Ferrer and M. Fernández-Garcia, *Appl. Catal., B*, 2018, **228**, 113–129.
61 D. Liu, Y. Xu, M. Sun, Y. Huang, Y. Yu and B. Zhang, *J. Mater. Chem. A*, 2020, **8**, 1077–1083.
62 J. Zhang, J. Liu, X. Wang, J. Mai, W. Zhao, Z. Ding and Y. Fang, *Appl. Catal., B*, 2019, **259**, 118063.
63 N. Lu, Z. Zhang, Y. Wang, B. Liu, L. Guo, L. Wang, J. Huang, K. Liu and B. Dong, *Appl. Catal., B*, 2018, **233**, 19–25.
64 J. Zhang, J. Liu, W. Zhao, Z. Ding, J. Mai and Y. Fang, *J. Alloys Compd.*, 2018, **764**, 1–9.

65 H. Liang, H. Zou and S. Hu, *New J. Chem.*, 2017, **41**, 8920–8926.
66 Z. Zhang, Y. Liu, Y. Fang, B. Cao, J. Huang, K. Liu and B. Dong, *Adv. Sci.*, 2018, **5**, 1800748.
67 Q. Huang, S. Hu, J. Zhuang and X. Wang, *Chem. – Eur. J.*, 2012, **18**, 15283–15287.
68 S. Balendhran, S. Walia, H. Nili, J. Z. Ou, S. Zhuiykov, R. B. Kaner, S. Sriram, M. Bhaskaran and K. Kalantar-zadeh, *Adv. Funct. Mater.*, 2013, **23**, 3952–3970.
69 J. Li, Y. Ye, L. Ye, F. Su, Z. Ma, J. Huang, H. Xie, D. E. Doronkin, A. Zimina, J. D. Grunwaldt and Y. Zhou, *J. Mater. Chem. A*, 2019, **7**, 2821–2830.
70 Y. Kuwahara, Y. Yoshimura, K. Haematsu and H. Yamashita, *J. Am. Chem. Soc.*, 2018, **140**, 9203–9210.
71 H. Cheng, M. Wen, X. Ma, Y. Kuwahara, K. Mori, Y. Dai, B. Huang and H. Yamashita, *J. Am. Chem. Soc.*, 2016, **138**, 9316–9324.
72 J. Shang, X. Xu, K. Liu, Y. Bao, Yangyang and M. He, *Ceram. Int.*, 2019, **45**, 16625–16630.
73 J. Li, X. Xu, B. Huang, Z. Lou and B. Li, *ACS Appl. Mater. Interfaces*, 2021, **13**, 10047–10053.
74 Y. Pan, S. Deng, L. Polavarapu, N. Gao, P. Yuan, C. H. Sow and Q.-H. Xu, *Langmuir*, 2012, **28**, 12304–12310.
75 J. Xiong, Z. Li, J. Chen, S. Zhang, L. Wang and S. Dou, *ACS Appl. Mater. Interfaces*, 2014, **6**, 15716–15725.
76 S. Ren, B. Wang, H. Zhang, P. Ding and Q. Wang, *ACS Appl. Mater. Interfaces*, 2015, **7**, 4066–4074.
77 Y. Zheng, L. Zhang, J. Guan, S. Qian, Z. Zhang, C. K. Ngaw, S. Wan, S. Wang, J. Lin and Y. Wang, *ACS Sustainable Chem. Eng.*, 2021, **9**, 1754–1761.
78 H. Robatjazi, H. Zhao, D. F. Swearer, N. J. Hogan, L. Zhou, A. Alabastri, M. J. McClain, P. Nordlander and N. J. Halas, *Nat. Commun.*, 2017, **8**, 1–10.
79 K. Wang, R. Jiang, T. Peng, X. Chen, W. Dai and X. Fu, *Appl. Catal., B*, 2019, **256**, 117780.
80 D. Mateo, J. Albero and H. García, *Energy Environ. Sci.*, 2017, **10**, 2392–2400.
81 Y. Lou, Y. Zhang, L. Cheng, J. Chen and Y. Zhao, *ChemSusChem*, 2018, **11**, 1505–1511.
82 M. Ai, J. Zhang, Y. Wu, L. Pan, C. Shi and J. Zou, *Chem. - Asian J.*, 2020, **15**, 3599–3619.
83 S. Lettieri, M. Pavone, A. Fioravanti, L. Santamaria Amato and P. Maddalena, *Materials*, 2021, **14**, 1645.
84 Y. Wang, T. Zhou, K. Jiang, P. Da, Z. Peng, J. Tang, B. Kong, W. Bin Cai, Z. Yang and G. Zheng, *Adv. Energy Mater.*, 2014, **4**, 1–7.
85 L. Lan, Z. Shi, Q. Zhang, Y. Li, Y. Yang, S. Wu and X. Zhao, *J. Mater. Chem. A*, 2018, **6**, 7194–7205.
86 Y. Zheng, W. Wang, D. Jiang, L. Zhang, X. Li and Z. Wang, *J. Mater. Chem. A*, 2016, **4**, 105–112.
87 Z. Shi, L. Lan, Y. Li, Y. Yang, Q. Zhang, J. Wu, G. Zhang and X. Zhao, *ACS Sustainable Chem. Eng.*, 2018, **6**, 16503–16514.
88 X. Chen, J. J. Li, X. Chen, S. C. Cai, E. Q. Yu, J. Chen and H. Jia, *ACS Appl. Nano Mater.*, 2018, **1**, 2971–2981.
89 Z. Lou, D. Yuan, F. Zhang, Y. Wang, Y. Li and L. Zhu, *Nano Energy*, 2019, **62**, 653–659.
90 Y. Li, C. Wang, M. Song, D. Li, X. Zhang and Y. Liu, *Appl. Catal., B*, 2019, **243**, 760–770.
91 Y. Zheng, W. Wang, D. Jiang and L. Zhang, *Chem. Eng. J.*, 2016, **284**, 21–27.
92 G. D. Zhou and Y. L. Duan, *The Basis of Structural Chemistry*, Peking Univ. Press, Peking, China, 2008, pp. 1–363.
93 S. Zhao, X. Jin, P. Wu, Y. Zhao, G. Chen, Y. Li, A. Li, D. Ye and Y. Qiu, *ACS Appl. Nano Mater.*, 2020, **3**, 10454–10461.
94 X. Chen, S. Cai, E. Yu, J. Li, J. Chen and H. Jia, *Appl. Surf. Sci.*, 2019, **484**, 479–488.
95 X. Zheng, G. Zhang, Z. Yao, Y. Zheng, L. Shen, F. Liu, Y. Cao, S. Liang, Y. Xiao and L. Jiang, *J. Hazard. Mater.*, 2021, **411**, 125180.
96 Y. Yang, Y. Li, M. Mao, M. Zeng and X. Zhao, *ACS Appl. Mater. Interfaces*, 2017, **9**, 2350–2357.
97 E. Yu, J. Li, J. Chen, J. Chen, Z. Hong and H. Jia, *J. Hazard. Mater.*, 2020, **388**, 121800.
98 C. Chen, Y. Li, Y. Yang, Q. Zhang, J. Wu, X. Xie, Z. Shi and X. Zhao, *Environ. Sci.: Nano*, 2019, **6**, 1233–1245.
99 Y. Yang, Y. Li, M. Zeng, M. Mao, L. Lan, H. Liu, J. Chen and X. Zhao, *Appl. Catal., B*, 2018, **224**, 751–760.
100 D. Xia, H. Liu, B. Xu, Y. Wang, Y. Liao, Y. Huang, L. Ye, C. He, P. K. Wong and R. Qiu, *Appl. Catal., B*, 2019, **245**, 177–189.
101 Y. Yang, S. Wu, Y. Li, Q. Zhang and X. Zhao, *J. Mater. Chem. A*, 2020, **8**, 1254–1264.
102 Y. Ma, Y. Li, M. Mao, J. Hou, M. Zeng and X. Zhao, *J. Mater. Chem. A*, 2015, **3**, 5509–5516.
103 L. Lan, Y. Li, M. Zeng, M. Mao, L. Ren, Y. Yang, H. Liu, L. Yun and X. Zhao, *Appl. Catal., B*, 2017, **203**, 494–504.
104 C. Ren, L. Zhou, Y. Duan and Y. Chen, *J. Rare Earths*, 2012, **30**, 1106–1111.
105 Z. Wang, H. Yu, Y. Xiao, L. Zhang, L. Guo, L. Zhang and X. Dong, *Chem. Eng. J.*, 2020, **394**, 125014.
106 Z. Wang, H. Yu, Y. Xiao, L. Guo, L. Zhang and X. Dong, *J. Hazard. Mater.*, 2021, **407**, 124795.
107 J. Hou, L. Liu, Y. Li, M. Mao, H. Lv and X. Zhao, *Environ. Sci. Technol.*, 2013, **47**, 13730–13736.
108 R. Verma, S. K. Samdarshi, S. Bojja, S. Paul and B. Choudhury, *Sol. Energy Mater. Sol. Cells*, 2015, **141**, 414–422.
109 M. Zeng, Y. Li, M. Mao, J. Bai, L. Ren and X. Zhao, *ACS Catal.*, 2015, **5**, 3278–3286.
110 Y. Li, Q. Sun, M. Kong, W. Shi, J. Huang, J. Tang and X. Zhao, *J. Phys. Chem. C*, 2011, **115**, 14050–14057.
111 G. Trovarelli, A. de Leitenburg and C. Dolcetti, *CHEMTECH*, 1997, **27**, 32–37.
112 P. Min, S. Zhang, Y. Xu and R. Li, *Appl. Surf. Sci.*, 2018, **448**, 435–443.
113 M. Bellardita, R. Fiorenza, L. D'Urso, L. Spitaleri, A. Gulino, G. Compagnini, S. Scirè and L. Palmisano, *Catalysts*, 2020, **10**, 765.
114 H. Liu, Y. Li, Y. Yang, M. Mao, M. Zeng, L. Lan, L. Yun and X. Zhao, *J. Mater. Chem. A*, 2016, **4**, 9890–9899.
115 M. J. Muñoz-Batista, A. M. Eslava-Castillo, A. Kubacka and M. Fernández-García, *Appl. Catal., B*, 2018, **225**, 298–306.

116 H. Liu, Y. Li, Y. Yang, Z. Shi, Q. Zhang, S. Wu and X. Zhao, *Catal. Today*, 2019, **326**, 46–53.
117 J. Hou, Y. Li, M. Mao, Y. Yue, G. Neville Greaves and X. Zhao, *Nanoscale*, 2015, **7**, 2633–2640.
118 J. Hou, Y. Li, M. Mao, X. Zhao and Y. Yue, *Nanoscale*, 2014, **6**, 15048–15058.
119 Q. Zhang, M. Mao, Y. Li, Y. Yang, H. Huang, Z. Jiang, Q. Hu, S. Wu and X. Zhao, *Appl. Catal., B*, 2018, **239**, 555–564.
120 M. Mao, Y. Li, H. Lv, J. Hou, M. Zeng, L. Ren, H. Huang and X. Zhao, *Environ. Sci.: Nano*, 2017, **4**, 373–384.
121 B. Liu, T. Xu, C. Li and J. Bai, *New J. Chem.*, 2020, **44**, 3794–3801.
122 M. Mao, Q. Zhang, Y. Yang, Y. Li, H. Huang, Z. Jiang, Q. Hu and X. Zhao, *Green Chem.*, 2018, **20**, 2857–2869.
123 U. Caudillo-Flores, I. Barba-Nieto, M. J. Muñoz-Batista, D. Motta Meira, M. Fernández-García and A. Kubacka, *Chem. Eng. J.*, 2021, **425**, 130641.
124 R. He, S. Cao, P. Zhou and J. Yu, *Cuihua Xuebao*, 2014, **35**, 989–1007.
125 J. Li, X. Wu, W. Pan, G. Zhang and H. Chen, *Angew. Chem., Int. Ed.*, 2018, **57**, 491–495.
126 H. Liu, R. Cheng, X. Dong, S. Zhu, R. Zhou, L. Yan, C. Zhang, Q. Wang, Z. Gu and Y. Zhao, *Inorg. Chem.*, 2020, **59**, 3482–3493.
127 M. Vanneman and G. Dranoff, *Nat. Rev. Cancer*, 2012, **12**, 237–251.
128 S. Her, D. A. Jaffray and C. Allen, *Adv. Drug Delivery Rev.*, 2017, **109**, 84–101.
129 J. Li, J. Wang, G. Zhang, Y. Li and K. Wang, *Appl. Catal., B*, 2018, **234**, 167–177.
130 S. Zhang, S. Zhang and L. Song, *Appl. Catal., B*, 2014, **152–153**, 129–139.
131 C. Yu, Z. Wu, R. Liu, D. D. Dionysiou, K. Yang, C. Wang and H. Liu, *Appl. Catal., B*, 2017, **209**, 1–11.
132 Y. Jia, S. Li, H. Ma, J. Gao, G. Zhu, F. Zhang, J. Y. Park, S. Cha, J. S. Bae and C. Liu, *J. Hazard. Mater.*, 2020, **382**, 121121.
133 J. Li, Y. Li, G. Zhang, H. Huang and X. Wu, *ACS Appl. Mater. Interfaces*, 2019, **11**, 7112–7122.
134 D. Jiang, W. Wang, E. Gao, L. Zhang and S. Sun, *J. Phys. Chem. C*, 2013, **117**, 24242–24249.
135 L. Wang, M. Ghoussoub, H. Wang, Y. Shao, W. Sun, A. A. Tountas, T. E. Wood, H. Li, J. Y. Y. Loh, Y. Dong, M. Xia, Y. Li, S. Wang, J. Jia, C. Qiu, C. Qian, N. P. Kherani, L. He, X. Zhang and G. A. Ozin, *Joule*, 2018, **2**, 1369–1381.
136 L. Wang, Y. Dong, T. Yan, Z. Hu, A. A. Jelle, D. M. Meira, P. N. Duchesne, J. Y. Y. Loh, C. Qiu, E. E. Storey, Y. Xu, W. Sun, M. Ghoussoub, N. P. Kherani, A. S. Helmy and G. A. Ozin, *Nat. Commun.*, 2020, **11**, 2432.
137 Y. Qi, L. Song, S. Ouyang, X. Liang, S. Ning, Q. Zhang and J. Ye, *Adv. Mater.*, 2020, **32**, 1903915.
138 A. Mohan, U. Ulmer, L. Hurtado, J. Loh, Y. F. Li, A. A. Tountas, C. Krevert, C. Chan, Y. Liang, P. Brodersen, M. M. Sain and G. A. Ozin, *ACS Appl. Mater. Interfaces*, 2020, **12**, 33613–33620.
139 Y. Li, J. Hao, H. Song, F. Zhang, X. Bai, X. Meng, H. Zhang, S. Wang, Y. Hu and J. Ye, *Nat. Commun.*, 2019, **10**, 2359.
140 A. A. Jelle, K. K. Ghuman, P. G. O'Brien, M. Hmadeh, A. Sandhel, D. D. Perovic, C. V. Singh, C. A. Mims and G. A. Ozin, *Adv. Energy Mater.*, 2018, **8**, 1702277.
141 Y. Chen, G. Zhu, M. Hojamberdiev, J. Gao, R. Zhu, C. Wang, X. Wei and P. Liu, *J. Hazard. Mater.*, 2018, **344**, 42–54.
142 A. Gannoruwa, K. Niroshan, O. A. Ileperuma and J. Bandara, *Int. J. Hydrogen Energy*, 2014, **39**, 15411–15415.
143 N. Wei, H. Cui, Q. Song, L. Zhang, X. Song, K. Wang, Y. Zhang, J. Li, J. Wen and J. Tian, *Appl. Catal., B*, 2016, **198**, 83–90.
144 M. J. Muñoz-Batista, M. M. Ballari, A. Kubacka, O. M. Alfano and M. Fernández-García, *Chem. Soc. Rev.*, 2019, **48**, 637–682.
145 M. Fracchia, P. Ghigna, A. Vertova, S. Rondinini and A. Minguzzi, *Surfaces*, 2018, **1**, 138–150.
146 U. Caudillo-Flores, M. J. Muñoz-Batista, A. Kubacka and M. Fernández-García, *ChemPhotoChem*, 2018, **2**, 777–785.
147 U. Caudillo-Flores, I. Barba-Nieto, M. J. Muñoz-Batista, A. Kubacka and M. Fernández-García, *Top. Curr. Chem.*, 2019, **377**, 24.
148 C. Kranz and M. Wächtler, *Chem. Soc. Rev.*, 2021, **50**, 1407–1437.
149 R. Ma, J. Sun, D. H. Li and J. J. Wei, *J. Catal.*, 2020, **392**, 165–174.

